High Schmidt number "Washout" of a soluble contaminant downstream of a backward-facing step

Dahhea Min[a], Paul F. Fischer[a,b], Arne J. Pearlstein[a,*]

[a] Department of Mechanical Science and Engineering, University of Illinois at Urbana-Champaign, Urbana, IL 61801, USA
[b] Department of Computer Science, University of Illinois at Urbana-Champaign, Urbana, IL 61801, USA

ABSTRACT

We compute two-dimensional high Schmidt number mass transfer downstream of a backward-facing step in a laminar flow, in which a nonreactive solute is initially confined to a region adjacent to the step, with square cross-section and dimensions equal to the height of the step. For Reynolds numbers (*Re*; based on step height and far-field velocity) of 10 and 100, and for Schmidt numbers (*Sc*) of 7, 500, and 2650, we present concentration distributions in the fluid and on the surface, in addition to time histories for the maximum concentration in the domain and the amount of solute remaining upstream of various points in the domain. We show that the rate of removal of solute decreases strongly as the Schmidt number increases from 7 to 2650. For $Re = 100$ and $Sc = 500$ and 2650, there is a time in the washout process when the location of the maximum concentration shifts from the relatively inaccessible bottom corner behind the step, to a point in the interior of the recirculation zone downstream of the step. When the washout process is approximated by a single exponential in each of three temporal ranges, that shift is seen to be accompanied by a dramatic reduction in the rate at which the maximum concentration decays. The joint effects of the Reynolds and Schmidt numbers on the washout process are discussed.

© 2020 Elsevier Ltd. All rights reserved.

I. Introduction

Removal or chemical neutralization of soluble or suspended contaminants adjacent to a rough surface, or of contaminant adsorbed or attached to such a surface, is important in a number of applications, including cleaning of circuit boards and other electronic components, sanitization of walls and floors in hospitals, and washing of fresh produce.

In applications where a chemical sanitizing agent (e.g., sodium hypochlorite, chlorine dioxide, ozone, peroxyacetic acid) is applied to inactivate bacteria and other microbial forms attached to a surface, there is sometimes present a soluble material that reacts with and consumes the sanitizer. In these cases, failure to remove the soluble material from the near-surface region will result in less efficient microbial inactivation than might be expected, and require use of higher concentrations of the sanitizer to accomplish the desired result, resulting in increased sanitizer consumption, environmental burden, and disposal costs, as well as potential damage to the surface by the sanitizer, or unacceptable residual sanitizer levels on the surface. In other cases, residual sanitizing agent itself needs to be removed from the surface.

An application illustrating these scenarios is washing of fresh-cut produce [1] (e.g., bagged salad, or shredded lettuce and cabbage). Typically, fresh-cut produce enters a flume and contacts a 4 °C aqueous solution of a chemical sanitizer. After passage through one or two such flumes, the objective of which is microbial inactivation, the produce enters a final flume, where potable water rinse aims to remove sanitizer, and possibly reaction products of sanitizer with "organic exudate" (a solution of sugars, sugar acids, thiols, amines, proteins, cellulose, and other organic species) released from cutting "wounds" to the plant tissue [2], and which adheres to the tissue surface. Recent work [3] shows that in the most common situation, where the sanitizer is sodium hypochlorite, reaction with exudate leads to considerable consumption of sanitizer, with three adverse consequences. First, sanitizer is consumed, and is no longer available for microbial inactivation. Second, sanitizer consumption complicates regulation of sanitizer concentration in the wash water, where levels too low provide insufficient microbial inactivation and levels too high damage product. Third, the disinfection by-products (DBPs) of sanitizer reaction with organic exudate can include trihalomethanes, haloacetic acids, and chlorinated phenols, some of which are known endocrine disruptors or potential carcinogens. As a result, the European Union and the U.S. FDA strongly regulate use of several disinfectants in washing of fresh-cut produce [4-5]. From the preceding discussion,

* Corresponding author.
  E-mail address: ajp@illinois.edu (A.J. Pearlstein).

it is clear that safe and effective sanitization can significantly benefit from prior removal of soluble organic exudate adjacent to the surface [6].

To the extent that surface topography can shield microbial targets from sanitizer, or soluble contaminants (e.g., DBPs or residual sanitizer) from "washout," it is clear that topography can significantly affect sanitization and washing. The backward-facing step is particularly attractive, because this simple geometry allows for investigation of washout by a boundary layer flow of contaminant shielded by roughness or other topography. In the fresh-cut produce application, the surface topography is provided by natural ridges on the produce, as for example, on iceberg lettuce.

For Schmidt numbers representative of liquids, little previous work exists on mass transfer in laminar flows in any geometry or flow regime. Work related to heat or mass transfer behind a backward-facing step is almost entirely devoted to the heat transfer case, with Prandtl numbers less than 10 [7–10]. (Experimental sublimation of naphthalene used as a surrogate for heat transfer corresponds to smaller Schmidt numbers, e.g., 2.5 in [11].) The only work known to us related to mass transfer behind a backward-facing step is a paper in which the fluid undergoes combustion [12]. What little other work there is in other geometries for high Prandtl or Schmidt numbers is concerned with situations in which the flow is axisymmetric [13–15] or turbulent [16–18], or the Reynolds number is very small [19–20]. That work includes simulations of a) axisymmetric flow in circular tubes with a stenosis [13], aneurysm [14], or sudden expansion [15], all relevant to flow in large blood vessels; b) buoyant plumes by Kaminski and Jaupart [19] at Prandtl numbers up to 10^4 (with maximum Reynolds number of about 3) and Tran et al. [20] for Schmidt numbers up to 6×10^5 (with a maximum Reynolds number of 12); c) oscillatory turbulent channel flow with either heat transfer at Prandtl numbers up to 100 [16] or mass transfer at a Schmidt number of 1020 [17]; and d) electrochemical mass transfer (with first-order surface kinetics) behind a rectangular obstacle on a flat surface for Re up to 66.4, with $500 \leq Sc \leq 2000$ [21], and to a circular cylinder for Re up to 200 and $Sc = 2010$ [22]. We are aware of no work related to heat transfer for a backward-facing step for a liquid with high Prandtl number (e.g., very viscous silicone oils).

Here, we report a computational investigation of washout by a boundary layer flow over a backward-facing step, of a soluble species initially shielded by the step. We focus on the laminar regime, which is relevant in the applications of interest. The remainder of the paper is organized as follows. In §2, we briefly discuss the formulation and computational approach. The results are presented in §3, followed by a discussion in §4, and conclusions in §5.

2. Formulation and computational approach

2.1. Formulation

We consider unsteady two-dimensional convective mass transfer in a constant-density, constant-viscosity flow past a backward-facing step, as shown in Fig. 1, with the origin of the coordinate system at what we refer to as the bottom corner of the step. We refer to $x = 0$, $y = h$ as the top corner of the step. We assume binary Fickian diffusion with a constant diffusivity. The computational domain extends from $x = -L_u$ upstream of the step to L_d downstream, and from $y = h$ to y_∞ upstream of the step and from $y = 0$ to y_∞ downstream of the step.

For the concentration distribution $C(x, y, t)$ of solute (referred to below as "contaminant"), we enforce no-flux conditions on the solid surface, and impose

$$C(-L_u, y, t) = 0 \tag{1}$$

at the upstream computational boundary. For the Péclet numbers of interest ($Pe = PrSc \geq 70$), upstream diffusion at the computational inlet is negligible [23], and our inflow condition (1) will introduce no significant error. The boundary conditions on concentration at the outflow boundary $x = L_d$ and at $y = y_\infty$ are taken to be $D(\nabla C) \bullet \mathbf{n} = 0$. We defer discussion of the initial concentration distribution until after introduction of dimensionless variables.

The boundaries at $y = 0$, $y = h$, and $x = 0$ are taken to be no-slip. The velocity is taken to be initially zero in the interior of the domain, with a profile (for $t > 0$) at $x = -L_u$ specified by

$$\mathbf{u}(-L_u, y - h, t) = U_{x,\ Blasius}\left[(y - h)/\sqrt{L_B \nu/U_\infty} \right]\mathbf{e}_x \tag{2}$$

taken to be the x-component of the Blasius approximation for a flat-plate boundary layer [24]. Here, L_B (see §2.2) is the distance upstream of $x = -L_u$ at which is located the boundary layer's "virtual origin," where a uniform velocity produces the specified profile of the x-component at $x = -L_u$ (Eq. (2)), and U_∞ is the free-stream velocity. At the outflow boundary $x = L_d$, we impose the traction-free condition $-p\mathbf{n} + \nu[\nabla\mathbf{u} + (\nabla\mathbf{u})^T] \bullet \mathbf{n} = \mathbf{0}$. At $y = y_\infty$, the x-component of the velocity is taken to be independent of x, and the wall-normal component is taken to be zero. The unsteady nature of the flow is dictated by the fact that in applications, the contaminant is typically present before flow begins.

The governing equations in dimensional form are

$$\nabla \bullet \mathbf{u} = 0 \tag{3a}$$

$$\rho\left[\frac{\partial \mathbf{u}}{\partial t} + \mathbf{u} \bullet \nabla\mathbf{u} \right] = -\nabla p + \mu\nabla^2\mathbf{u} \tag{3b}$$

$$\frac{\partial C}{\partial t} + \mathbf{u} \bullet \nabla C = D\nabla^2 C \tag{3c}$$

The dimensionless equations are

$$\nabla \bullet \mathbf{v} = 0 \tag{4a}$$

$$\frac{\partial \mathbf{v}}{\partial \tau_U} + \mathbf{v} \bullet \nabla\mathbf{v} = -\nabla\Pi + \frac{1}{Re}\nabla^2\mathbf{v} \tag{4b}$$

$$\frac{\partial S}{\partial \tau_U} + \mathbf{v} \bullet \nabla S = \frac{1}{ReSc}\nabla^2 S \tag{4c}$$

where we have defined the dimensionless variables $\tau_U = U_\infty t/h$, $\eta = x/h$, $\xi = y/h$, $\mathbf{v} = \mathbf{u}/U_\infty$, $\Pi = p/(\rho U_\infty^2)$, and $S = C/C_i$, where C_i is the maximum concentration in the initial distribution. Unless subscripted, the Reynolds number $Re = U_\infty h/\nu$ is based on the step height h. The Schmidt number is defined by $Sc = \nu/D$. We nondimensionalize time using the convective time scale τ_U because for the Re and Sc values considered, even the smallest Péclet number Pe is sufficiently large that transport is dominated by convection. While Re can be varied by changing U_∞, h, or ν, in experiments it is frequently easiest to vary U_∞ while holding h and ν fixed. If we think of Re as being varied by changing U_∞, then the same dimensional time t at different Re values will correspond to different values of τ_U. Thus, to allow comparison of results at two Re, we define a viscous time scale $\tau_\nu = \nu t/h^2 = \tau_U/Re$, for which the dimensional times are equal at equal dimensionless times, regardless of Re, with figures and tables using the viscous time scale included in the Supplemental Material. If we think of varying Sc by changing the diffusion coefficient D, then the dimensional times are equal at equal values of the dimensionless convective times, and at equal viscous times, regardless of Sc.
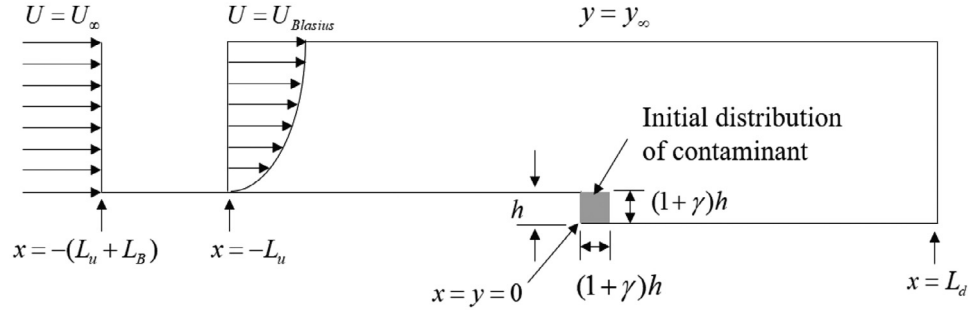
Fig. 1. Backward-facing step (of height h) configuration. Contaminant is initially confined to a faired portion of the square domain behind the step, with edge length $(1 + \gamma)h$.

In terms of these dimensionless variables, we choose the initial concentration distribution

$$S(\eta, \xi, 0) = \begin{cases} 1 & 0 \leq \max(\eta, \xi) \leq 1 - \gamma \\ f(\eta) & 1 - \gamma \leq \eta \leq 1 + \gamma, \ 0 \leq \xi \leq 1 - \gamma \\ f(\xi) & 0 \leq \eta \leq 1 - \gamma, \ 1 - \gamma \leq \xi \leq 1 + \gamma \\ f(\eta)f(\xi) & 1 - \gamma \leq \eta \leq 1 + \gamma, \ 1 - \gamma \leq \xi \leq 1 + \gamma \\ 0 & 1 + \gamma \leq \max(\eta, \xi) \end{cases}$$

(5)

where $f(\zeta) = (\zeta - 1 - \gamma)^2 (\zeta + 2\gamma - 1)/(4\gamma^3)$, which satisfies

$$\int_0^{1+\gamma} \int_0^{1+\gamma} S(\eta, \xi, 0) d\eta d\xi = 1$$

(6)

for all γ and is compatible with the no-flux boundary conditions on the walls. We use the "faired" or "smoothed" condition (Eq. (5)) rather than the simpler initial condition

$$S(\eta, \xi, 0) = \begin{cases} 1 & 0 \leq \max(\eta, \xi) \leq 1 \\ 0 & 1 < \max(\eta, \xi) \end{cases}$$

(7)

for two reasons. First, Eq. (5) avoids computational artifacts associated with the Gibbs phenomenon when a discontinuity in Eq. (7) or a near-discontinuity in the concentration distribution at small nonzero τ does not coincide with the boundary of a mesh element (i.e., at $\eta = 1$). Second, this approach is consistent with diffusion that inevitably occurs after a "sharp" interface is set up but before flow starts, even in careful laboratory experiments. Here, we use $\gamma = 0.02$.

2.2. Underlying flow

Our choice of Blasius profile corresponds to the boundary layer profile (Eq. (2)) at the computational inlet developing from a dimensional virtual origin $L_B = 22.574h$ upstream for $Re = 100$, and $L_B = 2.2574h$ upstream for $Re = 10$. For our approach to be relevant, it is necessary that the two-dimensional flow be stable. We are aware of no stability analysis for the starting or steady-state boundary layer flow over a backward-facing step (or relevant experimental data), but can make three observations. First, the steady boundary layer stability criterion $Re_{crit, \delta} = 500$ [25] (based on a displacement thickness $\delta = 4.91\sqrt{\nu x/U_\infty}$) leads to the conclusion that a steady two-dimensional boundary layer will be stable up to a distance $[(500/4.91)^2/Re]h$ downstream from its virtual origin. For $Re = 10$ and 100, this corresponds to distances of $103.7h$ and $1037h$, respectively, which exceed the corresponding values of $L_B + L_u$. Thus, the long-time flow will be stable upstream of the step. Second, Lanzerstorfer and Kuhlmann [26] considered stability of steady two-dimensional flow over a backward-facing step in a channel, with respect to infinitesimal two- and three-dimensional disturbances. For ten values of the channel height ratio $\Gamma = h/H$, where H is the downstream channel height, those authors computed the critical Reynolds number (denoted here by Re_{LK}) based

on one-half of the downstream channel height. Thus, we are interested in the limit of $2\Gamma Re_{LK}$ as $\Gamma \to 0$. From Table 3 of Ref. 22, we make two observations: a) the smallest value of $2\Gamma Re_{LK}$ at those Γ considered is about 563, with no reasonable curve fitted to the data yielding a minimum below 500, and b) $2\Gamma Re_{LK} \approx 2456$ at the smallest value of Γ considered, with $2\Gamma Re_{LK}$ increasing monotonically as Γ decreases below 0.7. These facts strongly suggest that steady two-dimensional flow upstream and downstream of the step in our flow will be stable. Finally, our unsteady two-dimensional computations give no indication of instability of the nominal flow with respect to two-dimensional disturbances.

For a step height of 1 mm in water at 4 °C, $Re = 10$ and 100 correspond to free-stream velocities of 1.57 and 15.7 cm s^{-1}, respectively.

2.3. Computational approach

As the Schmidt number increases, more spatial resolution is required. A particularly effective computational approach is the "spectral-element method," in which, spatial discretization is performed by approximating the dependent variables by bivariate polynomials (in two dimensions) on each element of a meshed domain [27]. Convergence can be achieved by either refining the mesh, or increasing the degree of the polynomial approximant, with asymptotic convergence in the latter case being exponential in the degree. For problems requiring high spatial resolution, this exponential convergence provides significant advantage over finite-volume, finite-difference, and finite-element techniques, for which the convergence rate is only polynomial in the number of mesh elements or grid points.

The governing equations are solved using Nek5000, an open-source, parallelized spectral-element code [28]. A so-called "$P_N - P_{N-2}$" spectral-element discretization is used [29], where N denotes the polynomial degree of the basis used to approximate the velocity, and the polynomial degree of the pressure approximation is lower by two.

Because the upstream flow is specified in terms of a boundary layer profile at a fixed upstream location, there is no upstream "computational boundary condition" at $x = -\infty$ that needs to be satisfied asymptotically, as would be the case for a bluff-body flow. We take $\eta_u = L_u/h = 40$.

We established the adequacy of the domain size, and of the spatial and temporal resolution, by comparing computed concentrations for the most challenging case ($Re = 100, Sc = 2650$) at points on the two boundaries which meet at the bottom corner, in each case one-half step height from that corner. The cross-stream and downstream extents ($\xi_\infty = y_\infty/h = 20$ and $\eta_d = L_d/h = 40$, respectively), time-step size ($(\Delta\tau)_U = 5 \times 10^{-4}$), number of mesh elements ($K = 1038$), and polynomial degree ($N = 19$, corresponding to $KN^2 = 374\,718$ grid points) provide adequate convergence (Tables S1(a,b) and S2(a,b)). The cross-stream extent $\xi_\infty = 20$ con-
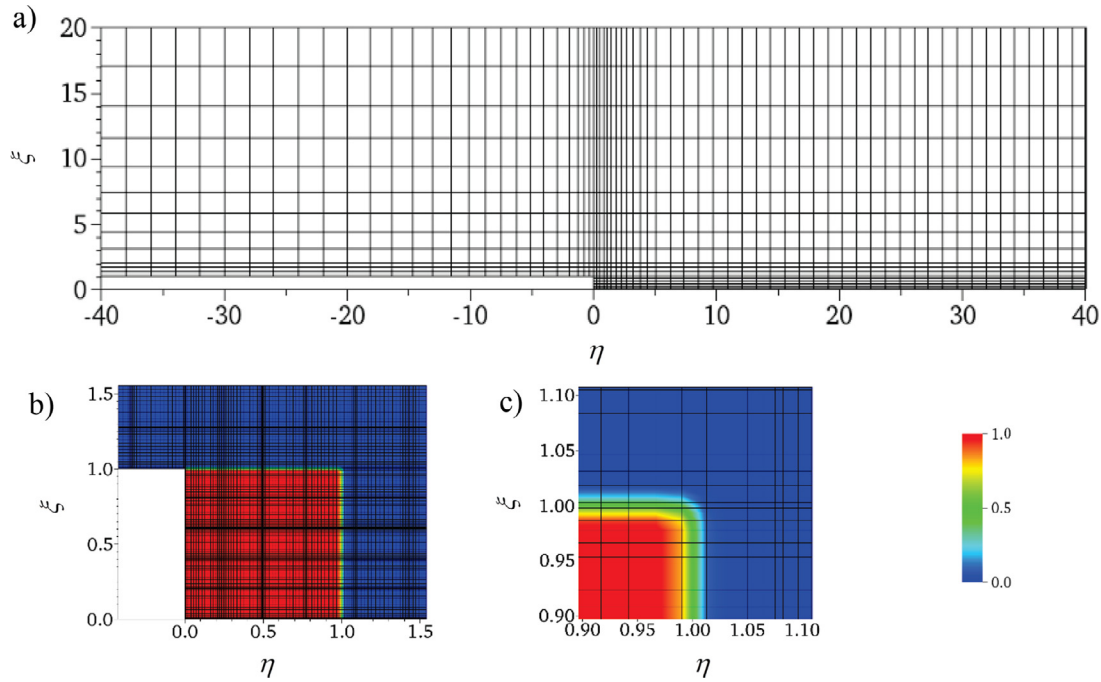
Fig. 2. a) 1038-element mesh for the entire computational domain; Gauss-Lobatto-Legendre points for $K = 1038$ and $N = 19$ showing the initial concentration distribution for b) the entire contaminated area behind the step; and c) the upper right, faired corner of the contaminated area. Blue and red represent 'fresh' and contaminated fluid, respectively. (For interpretation of the references to color in this figure legend, the reader is referred to the web version of this article.)

siderably exceeds the velocity boundary layer thickness ($\delta_{0.99}$), at $\eta = 40$ (the farthest point downstream, where $\delta_{0.99}$ is greatest), namely 10.3 and 4.6 at $Re = 10$ and $Re = 100$, respectively.

Fig. 2(a) shows the entire computational domain. The mesh, Gauss-Lobatto-Legendre points, and initial solute distribution are shown near the step in Fig. 2(b), and near the faired corner in Fig. 2(c).

We also compared results at $Re = 800$ for a somewhat different geometry (with the computational boundary at $\xi = \xi_\infty = 20$ replaced by a no-slip boundary at $\xi = 2$) to the benchmark results of Gresho et al. [30] at $Re = 800$ (again based on step height), using a computational domain identical to theirs. The results show that our flow computation is done with sufficient resolution to achieve convergence (see Table S3) for the dimensionless eddy length η_{LE}.

The assumption of constant density and viscosity allows "one-way decoupling", in which a well-resolved velocity field could be computed once for each Re, and then used as "input" to Eq. 4(c) for several Sc values following interpolation to the higher resolution required for the mass transfer computation. To avoid that interpolation and the resulting interpolation error, we instead compute the velocity field in each simulation at the same resolution needed for Eq. 4(c), and advance the solution of Eqs. 4(a,b) independently of Eq. 4(c) at each time step.

3. Results

Results were obtained for the case where $Re = 10$ or 100, and $Sc = 7$, 500, or 2650. Our largest Sc corresponds to the case of hypochlorite anion in water at 4 °C [31], and a kinematic viscosity of water obtained from Kestin et al. [32], and is typical of small ions at low temperatures, as well as of small molecules (e.g., sugars) at higher temperatures. The value $Sc = 500$ serves as a lower bound for small ions in aqueous solution near or above room temperature, and is more than an order of magnitude beyond the largest Pr considered in previous work on heat transfer with a backward-facing step [7-10]. The value $Sc = 7$ provides results corresponding to the Prandtl number for water.

The spatial variation of the concentration distributions below is displayed on a domain extending eight step heights downstream of the step, 1.8 step heights above the bottom corner of the step, and one step height upstream of the step. Surface distributions are displayed on a domain extending from one step height upstream of the (top corner of the) step to 18 step heights downstream of the (bottom corner of the) step. All distributions were computed on the much larger domain ($\eta_u = L_u/h = 40$, $\eta_d = L_d/h = 40$, $\xi_\infty = y_\infty/h = 20$) specified in §2.3.

3.1. $Re = 100$ and high Sc

Concentration distributions in the fluid. We begin with $Re = 100$, and show the time histories of the concentration field over the interval $0 \leq \tau_U \leq 2000$ (corresponding to about 12.7 s for a step height of 1 mm) for $Sc = 500$, and over $0 \leq \tau_U \leq 4000$ (corresponding to 25.4 s for the same step height) for $Sc = 2650$.

For $Sc = 500$, Fig. 3(a) shows that by $\tau_U = 0.5$, a "starting vortex" below the top corner of the step (at $\eta = 0$, $\xi = 1$) and a strong downward flow slightly downstream, have already developed. By $\tau_U = 1$, Fig. 3(b) shows that the vortex adjacent to the vertical face of the step has extended considerably downstream, and the initial material volume of high contaminant concentration has moved towards the $\xi = 0$ wall and downstream, with some of the contaminated fluid having been displaced by "clear" fluid that has flowed into the originally contaminated volume. The development of a green "border" (representing concentrations intermediate between fully contaminated fluid and "clear" fluid) shows that diffusion is beginning to play a role. (Absent diffusion, every point in the domain at each time would be red or blue.) By $\tau_U = 2$, Fig. 3(c) shows that the vortex has continued to grow in the η-direction, and the contaminant has been advected downstream. The fraction of the recirculation region essentially clear of contaminant increases as the reattachment point moves progressively downstream. The effects of diffusion have become more prominent, manifested in thinning of the red regions, and by the resulting growth of the green and yellow portions of the distribution, most evident on
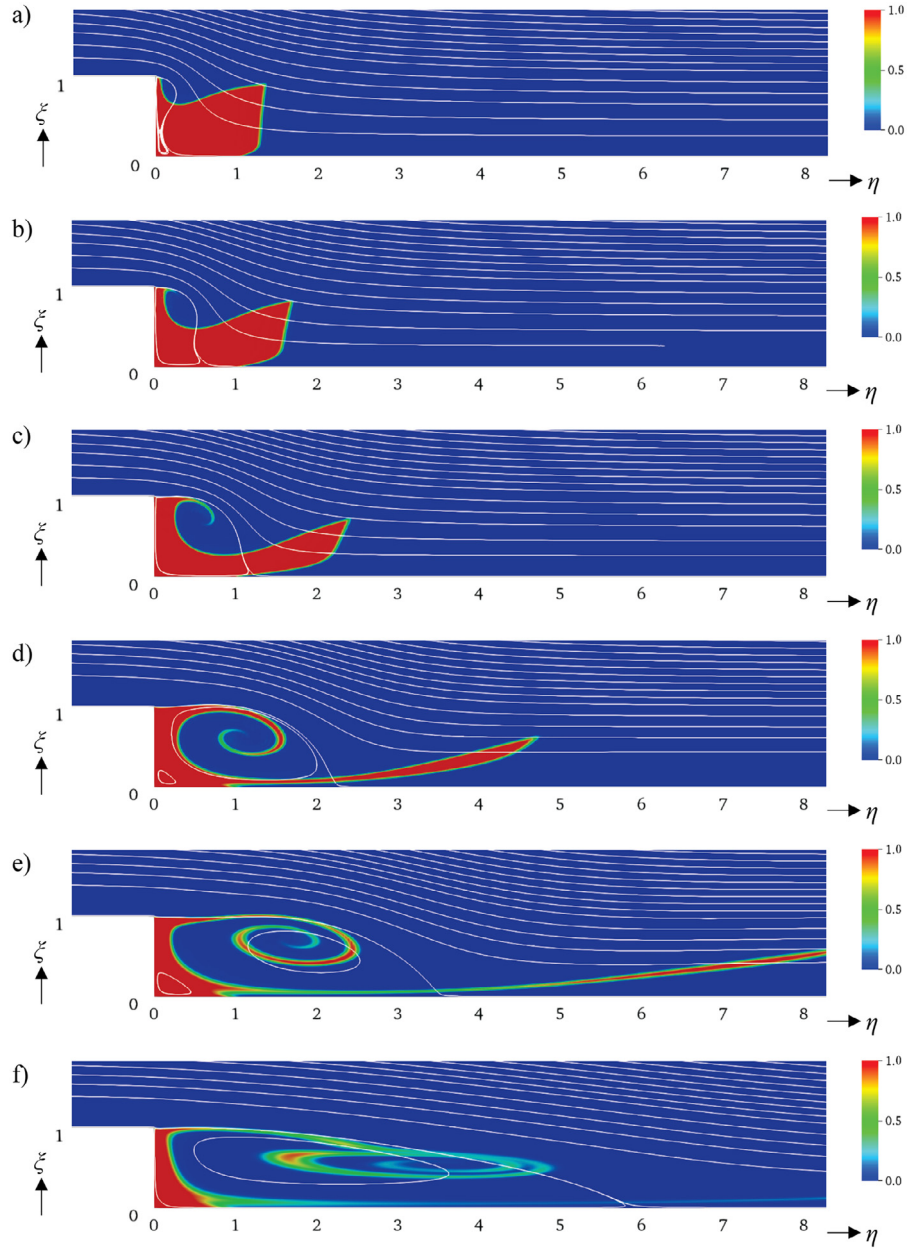
Fig. 3. Evolution of streamlines (white lines) and contaminant distributions for $Re = 100$ and $Sc = 500$ at a) $\tau_U = 0.5$, b) $\tau_U = 1$, c) $\tau_U = 2$, d) $\tau_U = 5$, e) $\tau_U = 10$, f) $\tau_U = 25$, g) $\tau_U = 50$, h) $\tau_U = 100$, i) $\tau_U = 250$, j) $\tau_U = 500$, k) $\tau_U = 1000$, l) $\tau_U = 2000$. (For interpretation of the references to color in this figure legend, the reader is referred to the web version of this article.)

the downstream boundary of the red contaminated zone. Fig. 3(d) shows that at $\tau_U = 5$, the recirculation zone has undergone significant elongation, and the secondary vortex near the bottom of the step has grown to the point where it is now apparent. The flow has led to a visible "roll-up" of the isoconcentration contours in the recirculation zone, extending into the core of the primary vortex. There is also strong distension of the contaminated fluid elements farthest downstream, due to a combination of two factors. First, at each location downstream of the reattachment point, there is a strong ξ-dependence of v_η, with contaminated fluid elements farther from the wall being carried downstream more rapidly than are elements closer to the $\xi = 0$ wall. Second, in the primary vortex, the "reverse" flow (with $v_\eta < 0$) adjacent to the $\xi = 0$ wall has the effect of transporting contaminant upstream, ultimately moving along the $\eta = 0$ wall toward the top corner of the step. The green and yellow regions have grown con-

siderably, being most prominent in the rolled-up region in the core of the primary vortex, where the contaminated fluid elements are thinnest.

At $\tau_U = 10$, Fig. 3(e) shows that the primary vortex has continued to elongate, with the most highly contaminated fluid still largely confined to a small region adjacent to the $\eta = 0$ face of the step, which region includes the secondary vortex. The high concentrations in the recirculation zone and downstream of it have been greatly reduced by diffusion acting on the thin elements of contaminated fluid downstream of the top corner of the step. While some contaminant has been washed out of the domain shown in Fig. 3(e), essentially all contaminant is still in the computational domain (with downstream boundary at $\eta = 40$). In the recirculation zone, the most highly contaminated fluid elements are very thin, and in the flow downstream of the separation point, the fluid elements that were the most highly contaminated are now less
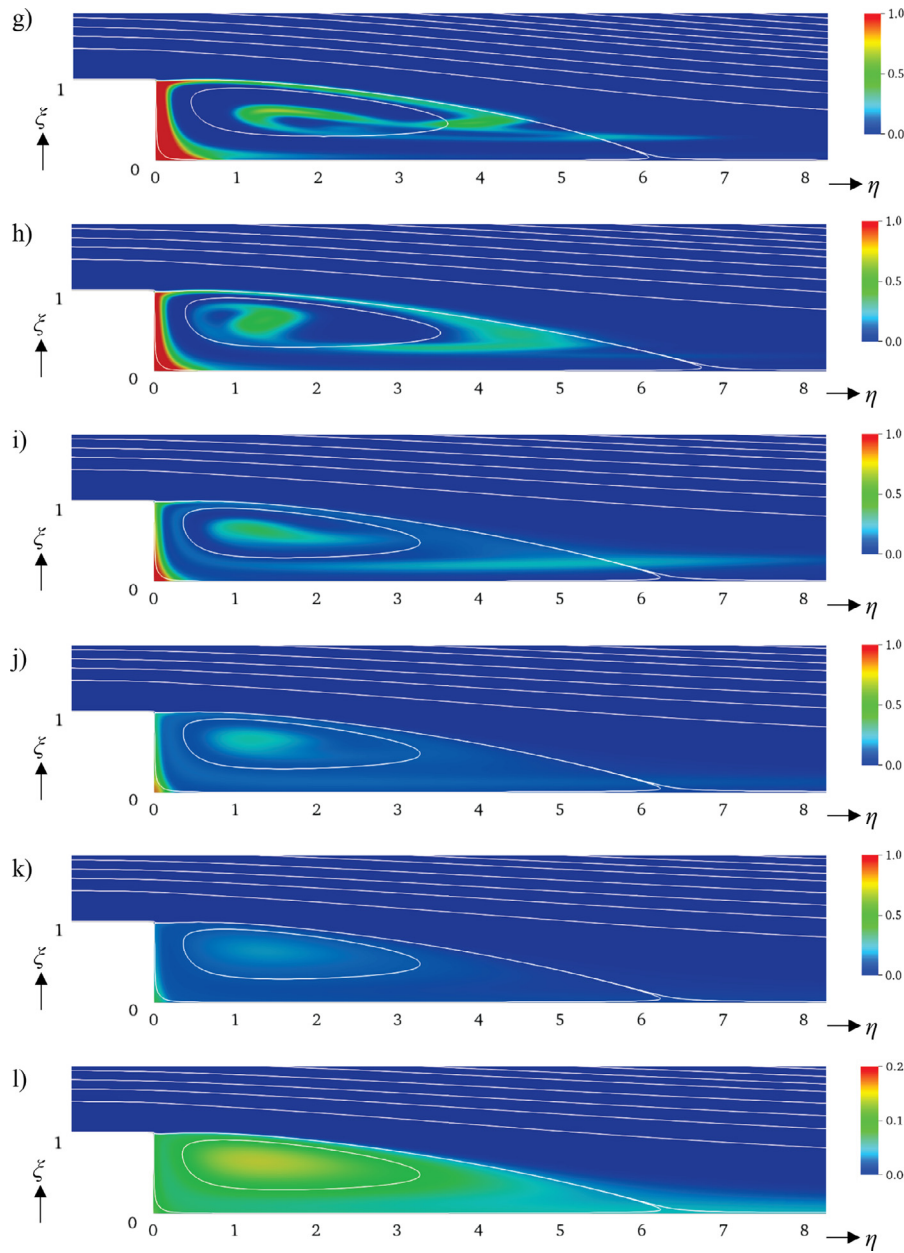
Fig. 3. Continued

contaminated, due to their distension and the subsequent effect of diffusion.

At $\tau_U = 25$, Fig. 3(f) shows that the vortex has continued to elongate, with rolled-up isoconcentration contours being carried downstream. The rolled-up region is "fed" by fluid that has traveled past the most highly contaminated zone near the $\eta = 0$ face, from which zone contaminant diffuses, and is then convected downstream from the top corner of the step. But the contaminated "filament" extending downstream from that corner along the separation streamline is so thin that diffusion efficiently reduces the maximum concentration to levels well below the maximum adjacent to the $\eta = 0$ wall. Transport of contaminant across the separation streamline is the result of two effects. First, at any instant, contaminant can diffuse across a streamline. In addition, the separation streamline here is unsteady, with its point farthest from the $\xi = 0$ wall at $\tau_U = 10$ (near $\eta = 1.5$, with $\xi > 1$) moving closer to the $\xi = 0$ wall as time advances, as shown in Figs. 3(e, f) and Supplemental Movie 1. The re-

sult is that fluid elements lying inside the recirculation zone at $\tau_U = 10$ will later lie outside that zone, where they are carried downstream. For $\tau_U < \eta_d$ and the large Pe values considered here, essentially all contaminant remains in the computational domain.

At $\tau_U = 50$, Fig. 3(g) shows that the most highly contaminated region, adjacent to the $\eta = 0$ wall, continues to diminish. At $\tau_U = 25$ and 50, a (green) region of contaminated fluid is connected to the rolled-up region in the core. This region extends farther downstream and closer to the $\xi = 0$ wall at $\tau_U = 50$. As shown in Supplemental Movie 1, this results from advection of contaminant that at $\tau_U = 25$ was already outside the separation streamline. The movie shows that inside the recirculation zone, the region of highest contaminant concentration is progressively reduced to a small zone at the bottom of the step as contaminant diffuses away from the $\eta = 0$ wall and into the primary vortex. Contaminant is carried along that wall towards the top corner of the step, and from there downstream, initially on the "vortex side" of the sep-
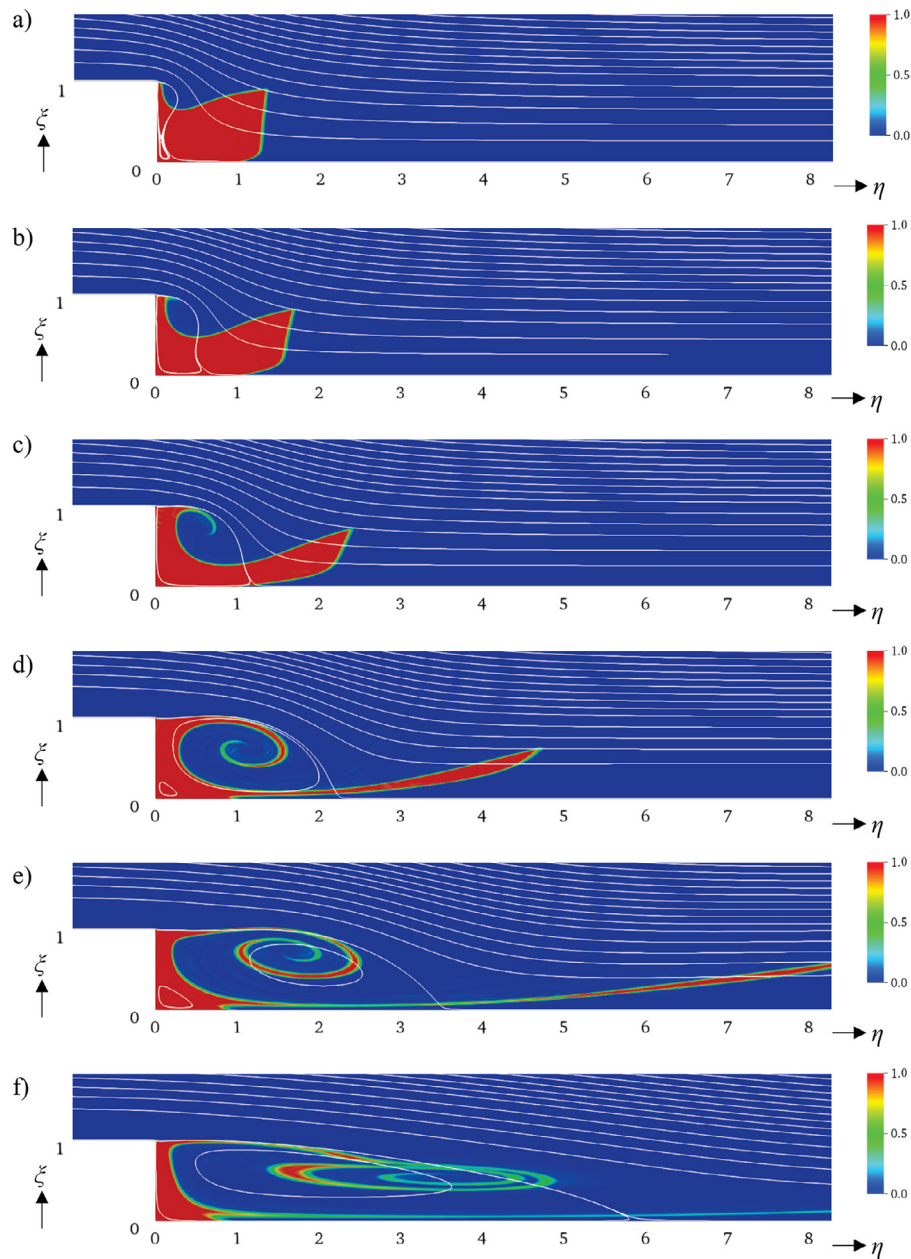
Fig. 4. Evolution of streamlines (white lines) and contaminant distributions for $Re = 100$ and $Sc = 2650$ at a) $\tau_U = 0.5$, b) $\tau_U = 1$, c) $\tau_U = 2$, d) $\tau_U = 5$, e) $\tau_U = 10$, f) $\tau_U = 25$, g) $\tau_U = 50$, h) $\tau_U = 100$, i) $\tau_U = 250$, j) $\tau_U = 500$, k) $\tau_U = 1000$, l) $\tau_U = 2000$. (For interpretation of the references to color in this figure legend, the reader is referred to the web version of this article.)

aration streamline. Contaminant that diffuses across the separation streamline, or is in fluid elements that pass out of the recirculation zone as part of the unsteady separation streamline moves towards the $\xi = 0$ wall, is carried downstream beyond the reattachment point. On the other hand, contaminant that has not passed across the separation streamline before reaching the vicinity of the reattachment point is then returned upstream along the $\xi = 0$ wall towards the step. Contaminant in the core of the primary vortex is subject to relatively less shear and is relatively far from the separation streamline, across which diffusion provides "escape".

For $Sc = 2650$, the results for small times (Figs. 4(a–d)) are graphically indistinguishable from those for $Sc = 500$, with only very slight differences being discernible at $\tau_U = 10$ (Fig. 4(e)). This is a consequence of the fact that at these two large values of Sc, diffusion has had insufficient time to play a significant role. For $25 \leq \tau_U \leq 2000$, Figs. 4(f–l) show that the contrasts to the

$Sc = 500$ case are increasingly apparent, with several features being particularly prominent. One of these is the greater persistence, at $\tau_U = 25$, of highly contaminated fluid in the recirculation region near $\eta = 1.7$, $\xi = 0.6$, compared to the $Sc = 500$ case (compare Figs. 3(f) and 4(f)). At still larger times, the concentration distributions for $Sc = 2650$ are more sharply defined than those for $Sc = 500$, and clearly show the effects of less diffusion. At very large times, comparison of Figs. 4(l) and 3(l) (both at $\tau_U = 2000$) shows that there is considerably more contaminant in the relatively well-mixed recirculation zone for $Sc = 2650$ than for $Sc = 500$. For $Sc = 2650$, the very slow reduction in remaining contaminant is a direct consequence of slower diffusion across the separation streamline. Supplemental Movie 2 shows that rotation and distension of the high-concentration region near the center of the recirculation zone is quite apparent in this higher-Sc case. (This is especially apparent for $60 \leq \tau_U \leq 200$).
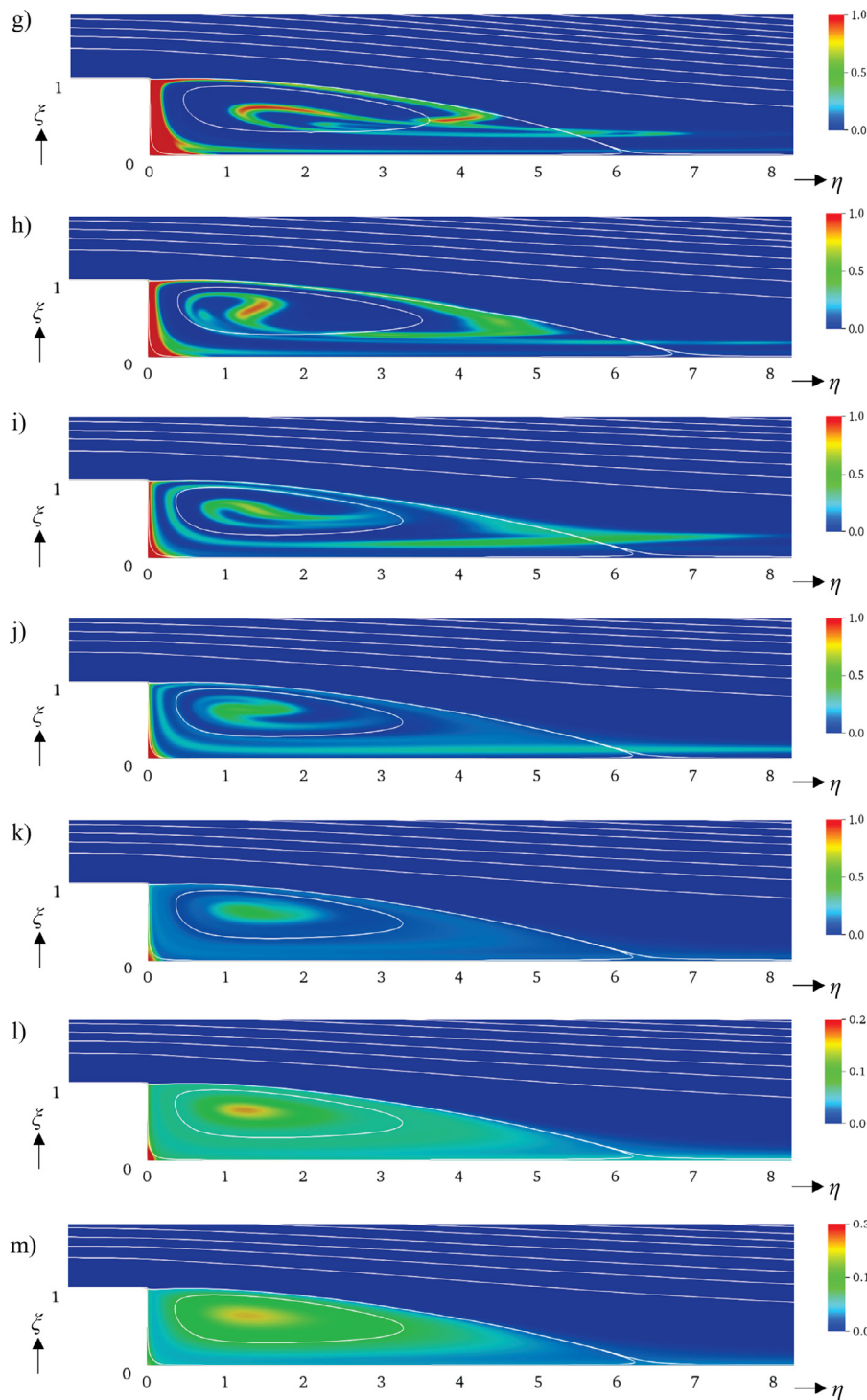
Fig. 4. Continued

Concentration distributions on the surface. In cases where a contaminant can damage or otherwise interact with a surface, it is important to know the spatiotemporal distribution of the contaminant on the surface. (Note that our analysis does not account for adsorption or chemical reaction at the surface, so that when such phenomena occur, the results presented here are only suggestive of possible effects.)

For $Re = 100$ and $Sc = 500$, we present surface concentration results using an arclength σ measured from the upstream computational inlet at $\eta = -40$, so that the top corner of the step is at

$\sigma = 40$, while the bottom corner is at $\sigma = 41$. Fig. 5(a) shows the time dependence of the surface distribution from one step height upstream of the step to 18 step heights downstream of the step (corresponding to $-1 \leq \eta \leq 0$ for $\xi = 1$, $0 \leq \xi \leq 1$ for $\eta = 0$, and $0 \leq \eta \leq 18$ for $\xi = 0$) for $0 \leq \tau_U \leq 2000$. When Pe is large (5×10^4 here), upstream diffusion is negligible, and the concentration upstream of the step is never significant. As contaminant is transported within the flow, the first portion of the surface to experience a reduction in concentration is just upstream of $\sigma = 42$ (essentially coincident with the downstream extent of the initial con-
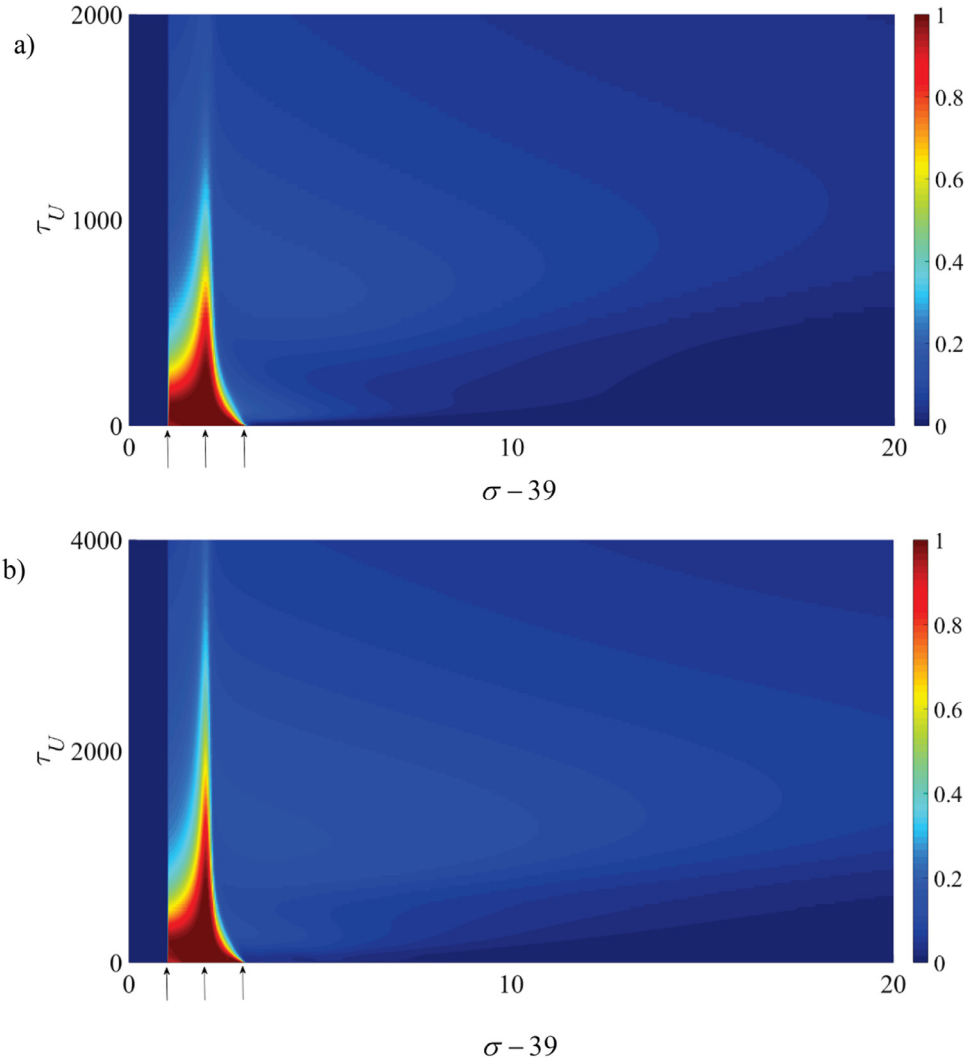
Fig. 5. For $Re = 100$ and a) $Sc = 500$ and b) $Sc = 2650$, time history of concentration along the wall. Left, center, and right arrows denote top corner of step (arclength $\sigma = 40$), bottom corner ($\sigma = 41$), and streamwise extent of initial contaminant distribution ($\sigma = 42$), respectively. Note the difference in time axes. (For interpretation of the references to color in this figure legend, the reader is referred to the web version of this article.)

taminant distribution on the $\xi = 0$ wall). Fig. 5(a) shows that high surface concentrations of contaminant never extend beyond that point. As time advances, the region of highest surface concentration is increasingly isolated near the bottom of the step ($\sigma = 41$).

For $Re = 100$ and $Sc = 2650$, Fig. 5(b) shows the spatiotemporal distribution of surface concentration. Comparison to Fig. 5(a) for $Sc = 500$ (note the difference in vertical scale between Figs. 5(a) and 5(b)) shows that the surface concentrations remain high much longer for the larger Sc. This comparison also shows that the two distributions are very similar if the dimensionless time is appropriately "stretched".

Maximum remaining concentration. From a practical standpoint, a key measure of washing efficacy is the time dependence of the maximum concentration (denoted by S_{max}). Fig. 6 (and Fig. S1 using the viscous time scale) shows that for $Re = 100$ and $Sc = 500$ and 2650, there is a time $\tau_{U, switch}$ (near 1580 and 3270 for $Sc = 500$ and 2650, respectively) at which the slope of the plot of S_{max} versus time changes abruptly. This change in slope occurs when the location of maximum concentration shifts from the bottom corner of the step to the interior of the recirculation zone. (This change in location is also discernible by comparing Fig. 3(k) to Fig. 3(l), and Fig. 4(l) to Fig. 4(m).) The effect is to move the

maximum concentration from a location where the shear rate is relatively high and the concentration gradient is large (at the bottom corner of the step), to a region in which the shear rate is lower and the concentration gradient is smaller (the core of the recirculation zone). Fitting exponential decay curves $S_{max, fit}^-(\tau_U) = A_- \exp(-\alpha_- \tau_U)$ to the time series for $\tau_{U, switch}/2 \leq \tau_U \leq \tau_{U, switch}$, and $S_{max, fit}^+(\tau_U) = A_+ \exp(-\alpha_+ \tau_U)$ for $\tau_{U, switch} \leq \tau_U \leq 8000$, we obtain the results shown in Table 1 (and Table S4 for the viscous time scale). It is apparent that after the location of maximum concentration moves from the bottom corner of the step to the interior of the recirculation zone, its decay rate decreases significantly. The absolute and relative rms errors associated with these exponential fits indicate that for the time intervals used to fit the decay, single exponential fits are satisfactory.

Integral measure of washout. A second key scalar measure of washing efficacy is the fraction of the contaminant remaining in some part of the domain. We define the fraction of contaminant remaining upstream of a streamwise position $\eta_e \leq \eta_d$ by

$$M(\tau_U; \eta_e) = \int_{-\eta_u}^{0} \int_{1}^{\xi_\infty} S(\eta, \xi, \tau_U) d\eta d\xi + \int_{0}^{\eta_e} \int_{0}^{\xi_\infty} S(\eta, \xi, \tau_U) d\eta d\xi \quad (8)$$
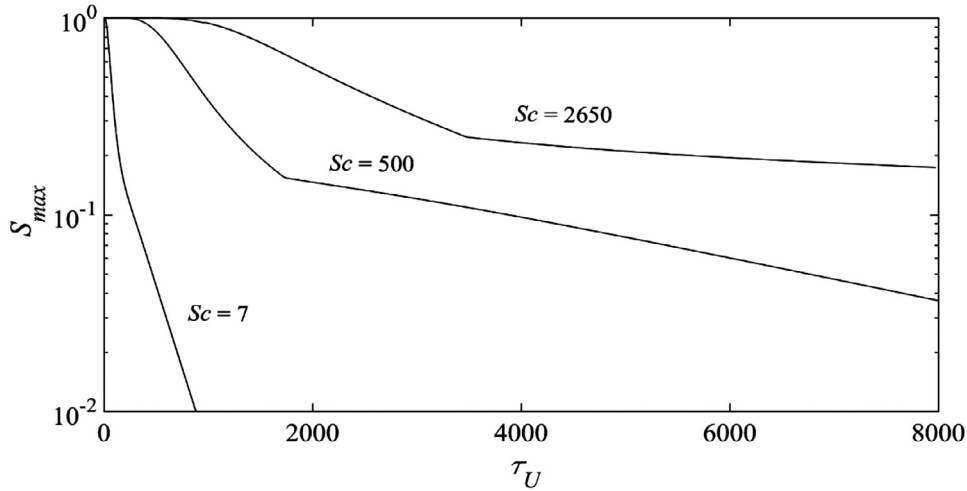
Fig. 6. Temporal variation of maximum councentration in the computational domain for $Re = 100$ and the three Schmidt numbers considered. Figure S1 presents these results using the viscous time scale τ_v.

Table 1
Exponential decay rates ($\alpha_\pm$) of the maximum concentration (S_{max}), and absolute and relative rms residuals between computed and fitted values of S_{max}, for $Re = 100$ with $Sc = 500$ ($\tau_{U,switch} = 1580$) and 2650 ($\tau_{U,switch} = 3270$).

		$Sc = 500$	$Sc = 2650$
$\tau_{U,\,switch}/2 \leq \tau_{U,\,switch}$	α_-	1.3558×10^{-3}	5.6805×10^{-4}
	$(S_{max} - S_{max,\,fit})_{rms}$	8.0802×10^{-3}	4.2519×10^{-3}
	$(1 - S_{max,\,fit}/S_{max})_{rms}$	3.5745×10^{-2}	1.2058×10^{-2}
$\tau_{U,\,switch} \leq \tau_U \leq 8000$	α_+	2.2486×10^{-4}	7.7772×10^{-5}
	$(S_{max} - S_{max,\,fit})_{rms}$	1.5989×10^{-3}	2.8019×10^{-3}
	$(1 - S_{max,\,fit}/S_{max})_{rms}$	2.3470×10^{-2}	1.3471×10^{-2}

where the contribution from the first (upstream) integral is very small.

For $Re = 100$ and $Sc = 500$, Fig. 7(a) (and Fig. S2(a) for the viscous time scale) shows the time dependence of M for several η_e. While it is clear that at each time the amount of material must increase monotonically with η_e, and that for sufficiently large times M decreases monotonically in time for all η_e, it is also true that for each η_e, there is a range of times below $\tau_U = 100$ ($\tau_v = 1$) in which M does not decrease monotonically with time. (The effect is shown more dramatically in Fig. S3(a), where the ordinate is linear, and the time scale is expanded.) The reason for this is that for times beyond those at which the reattachment point has passed η_e (Fig. S4), reverse flow in the recirculation zone, near the $\xi = 0$ wall, returns contaminant upstream. If η_e is upstream of the reattachment point at a given time, then $M(\tau_U; \eta_e)$ can increase over some interval of time. When contaminant in the recirculation zone is carried upstream, the effect can be large enough to overcome diffusion out of the recirculation region, across the separation streamline, and downstream advection by the free stream, which together have the effect of causing $M(\tau_U; \eta_e)$ to increase as τ_U increases. This is especially true for the smallest η_e considered, for which the reattachment point passes beyond η_e relatively early. For the largest values of η_e shown in Fig. 7(a), the reattachment point never reaches η_e, and decay of M with time is monotonic.

For $Re = 100$, Fig. 7(b) (and Fig. S2(b) for the viscous time scale) shows that washout is considerably slower at $Sc = 2650$ than at $Sc = 500$. (Nonmonotonic dependence of M on time, shown more clearly in Fig. S3(b) with a linear ordinate, has the same explanation as for $Sc = 500$, as discussed above in connection with Fig. 7(a).) For each τ_U and η_e, Fig. 7(b) shows that the fraction of contaminant remaining in a given portion of the domain (i.e., for the same η_e) is higher at $Sc = 2650$. Decay rates (see Tables S5(a,b)

for numerical values) for $Sc = 2650$ are about 40% lower than for $Sc = 500$. This is again a direct consequence of slower diffusion.

For $Sc = 500$ and 2650, Figs. 7(a,b) (and Figs. S2(a,b) for the viscous time scale) also show that following an initial transient, the temporal decay of M, measured on the time scale of the flow, is very slow. The asymptotic decay rates (computed by linear least-squares fitting of a single exponential in time to the logarithmically transformed data, for $\tau_U \geq 1000$) are nearly independent of η_e (within 2%) for $1 \leq \eta_e \leq 40$, as shown in Tables S5(a) and S5(b)) for $Sc = 500$ and 2650, respectively. The pre-exponential factors increase monotonically with η_e, reflecting the fact that at each time, the amount of material upstream of η_e is an increasing function of η_e. At each η_e, least-squares fitting of a straight-line time dependence ($c_1 - c_2\tau_U$) for $M(\tau_U; \eta_e)$ gives slopes very similar to those of the exponential decay, but with significantly larger rms errors over the duration of the time series. (Note that our least-squares fitting of an exponential model minimizes the sum of the squares of the deviations from $\ln M$, and that a non-linear least-squares approach minimizing the sum of the squares of the deviations in M would necessarily produce smaller rms values.)

The abrupt change in slope for the time dependence of the maximum concentration observed for $Sc = 500$ and 2650 (Fig. 6), associated with the change in location of maximum concentration, has no counterpart in the time dependence of M, because that change in location has no such effect on an integral property.

3.2. $Re = 10$ and high Sc

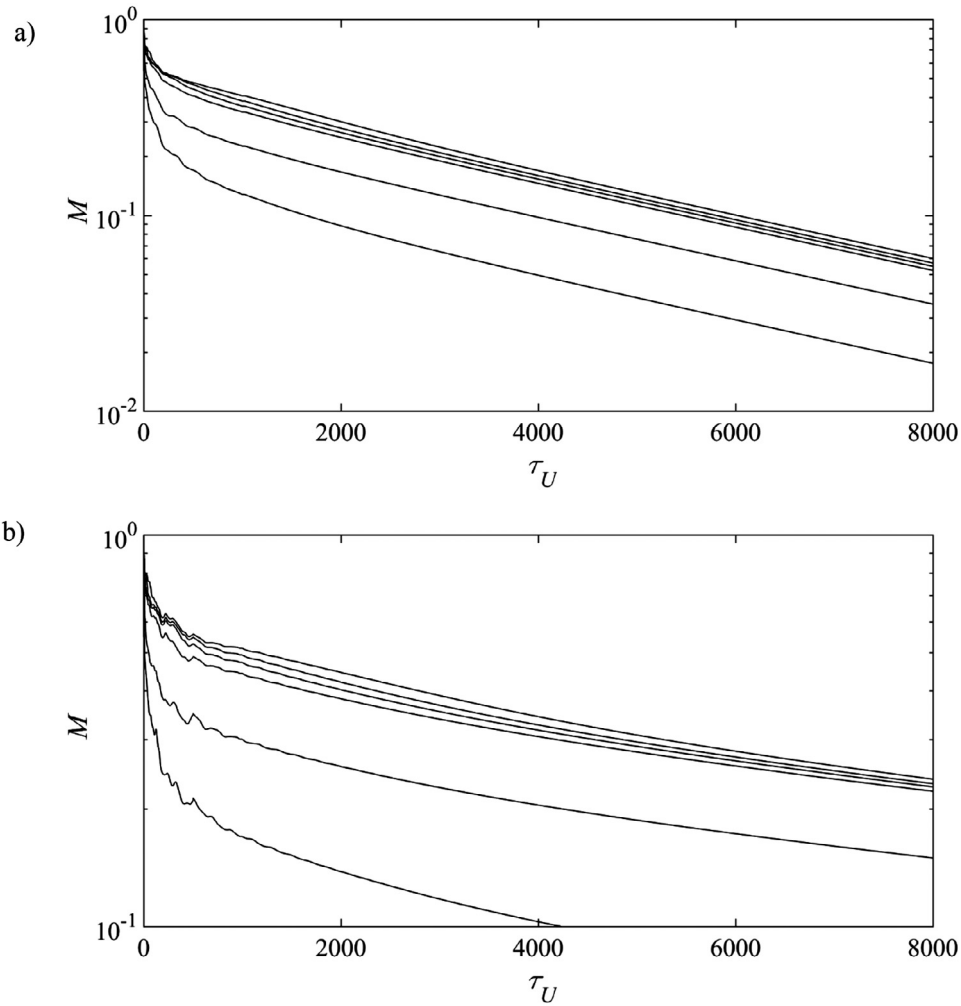To better understand Reynolds number effects, we performed a similar set of computations at $Re = 10$.

a)

b)

Fig. 7. For $Re = 100$ and a) $Sc = 500$ and b) $Sc = 2650$, time history of contaminant remaining upstream of a given η_e, for $\eta_e = 1$ (bottom curve), 2, 5, 10, 20, and 40 (top curve). Exponential decay rates and rms deviations for these η_e computed for $\tau_U \geq 1000$ are shown in Tables S5(a,b).

Concentration distributions in the fluid. For $Re = 10$ and $Sc = 500$, Figs. 8(a-n) show distributions of contaminant at increasing values of τ_U. At the earliest nonzero time ($\tau_U = 0.5$), Fig. 8(a) shows that the main effect has been for the velocity field to deform the material volume in which the contaminant was initially confined. We see that the upper surface of that material volume has been depressed by the downwardly directed flow downstream of the step (as indicated by the streamlines), and that the upper right part of this material volume has been carried slightly downstream. The green border of the red material volume shows that the thickness of the layer in which diffusion occurs is significant. Comparison of Figs. 8(a-n) to Figs. 3(a–l) shows that at $Re = 10$, the material volume of initially contaminated fluid has undergone significantly different deformation than in the $Re = 100$ case. The separation streamline divides the region of high contaminant concentration into parts that are inside and outside the recirculation zone. The thickness of the (yellow and green) diffusion layer separating fluid with high contaminant concentration from uncontaminated fluid becomes progressively thicker as τ_U increases. Fig. 8(e) (at $\tau_U = 5$) shows that the region of high concentration outside of the recirculation zone becomes increasingly distended. All of this early deformation is a direct consequence of the fact that downstream of the step and external to the recirculation zone, the velocity has a significant component towards the $\xi = 0$ wall, and becomes more nearly parallel to that wall farther downstream, as is clearly evident in Supplemental Movie 3. As the separation streamline moves farther from the bottom corner of the step to include more contaminant in the recirculation zone, and as the (red) region of high concentration outside the recirculation zone thins, a larger fraction of the contaminant in the external flow is within a diffusion thickness of uncontaminated fluid. This has the effect of rapidly decreasing the amount of highly contaminated fluid in the external flow, and leaves essentially all of the highly contaminated fluid inside the recirculation zone.

Figs. 8(f–n) and Supplemental Movie 3 show that the contaminant exterior to the recirculation zone continues to diffuse into the uncontaminated fluid, especially away from the $\xi = 0$ wall. Once the flow has nearly reached a steady state (say, by $\tau_U = 25$) and the separation streamline is no longer moving outward from the bottom corner of the step, the only way for contaminant to cross the separation streamline is by diffusion, which process progressively reduces the amount of contaminant in the recirculation zone. Moreover, the red region of highest contaminant concentration becomes progressively localized at the bottom corner of the step.

For $Re = 10$, comparison of Figs. 8(a–e) to Figs. 9(a–e) shows that for $\tau_U \leq 5$, the concentration distributions are very similar for $Sc = 500$ and 2650, with the only discernible difference being a slightly thicker diffuse interface between contaminated and uncontaminated fluid for the smaller Sc. At larger times,
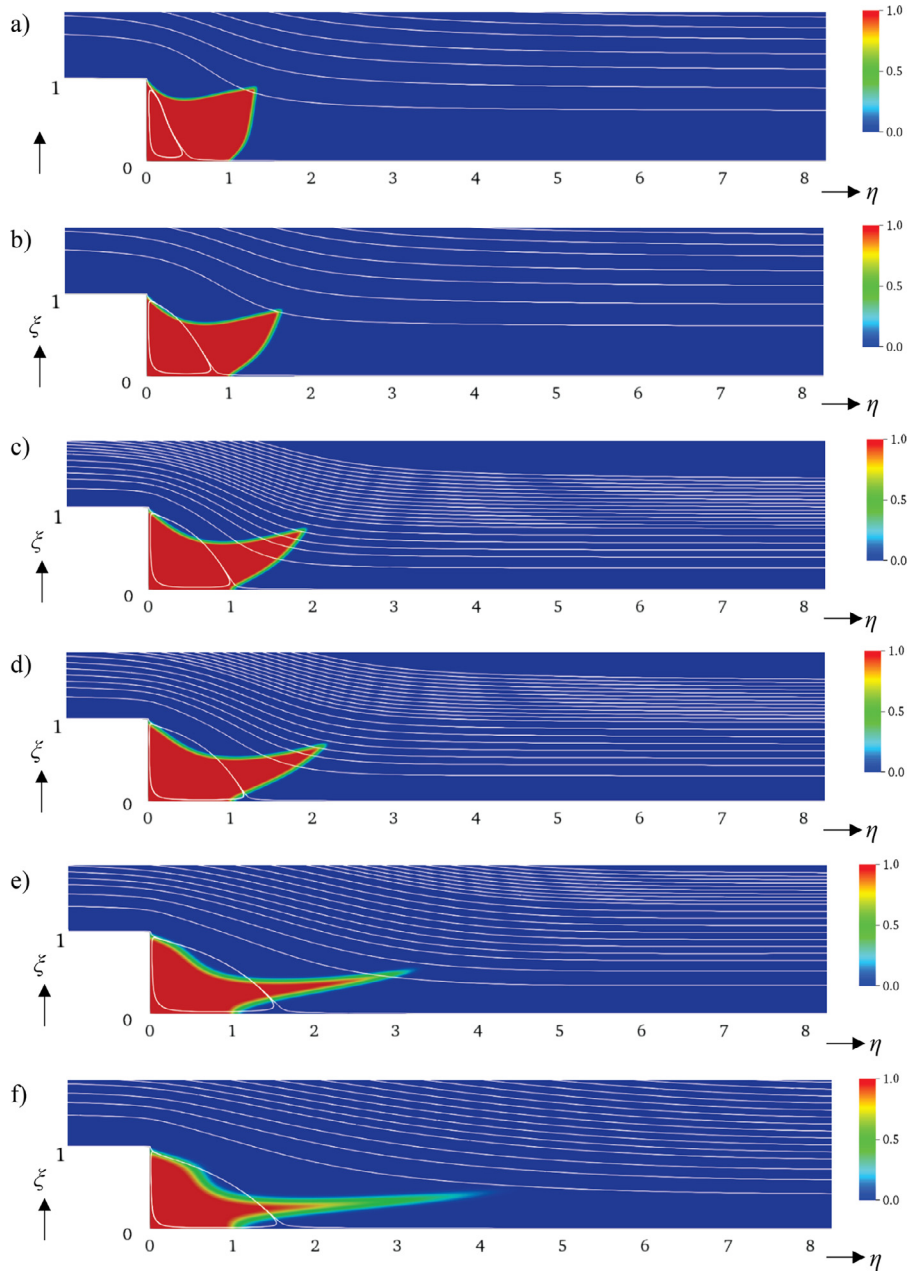
Fig. 8. Evolution of streamlines (white lines) and contaminant distributions for $Re = 10$ and $Sc = 500$ at a) $\tau_U = 0.5$, b) $\tau_U = 1$, c) $\tau_U = 1.5$, d) $\tau_U = 2$, e) $\tau_U = 5$, f) $\tau_U = 10$, g) $\tau_U = 25$, h) $\tau_U = 50$, i) $\tau_U = 100$, j) $\tau_U = 250$, k) $\tau_U = 500$, l) $\tau_U = 1000$, m) $\tau_U = 2000$, n) $\tau_U = 4000$. (For interpretation of the references to color in this figure legend, the reader is referred to the web version of this article.)

however, the differences become more pronounced, with a comparison of Figs. 8(j–n) to Figs. 9(j–n) showing that the region of significant contaminant concentration outside of the recirculation zone is considerably more diffuse at $Sc = 500$ than at $Sc = 2650$. Comparison of Supplemental Movies 3 and 4 shows that the concentration distribution inside the vortex has considerably more internal structure at $Sc = 2650$ than at $Sc = 500$, as expected given the relatively less important role played by diffusion at the higher Sc.

Comparing these $Re = 10$ results at $\tau_U = 0.5$ (Figs. 8(a) and 9(a) for $Sc = 500$ and 2650, respectively) to those for $Re = 100$ (Figs. 3(a) and 4(a) for $Sc = 500$ and 2650, respectively) at the same dimensionless (convective) time, we see that initial deformation of the contaminated material volume is qualitatively similar. But the relatively deeper penetration of the flow immediately be-

hind the step for $Re = 100$ produces a more pronounced depression of the upper boundary of the material volume of initially contaminated fluid than for $Re = 10$. Considering the case where Re is varied by changing U_∞, with h and ν held constant, we can compare results at the same dimensional time for $Re = 10$ and 100 by considering dimensionless times tenfold larger for the latter Re. Comparing results at $\tau_U = 0.5$ for $Re = 10$ and at $\tau_U = 5$ for $Re = 100$ (Figs. 8(a) and 3(d) for $Sc = 500$, and Figs. 9(a) and 4(d) for $Sc = 2650$), we see that the contaminated material volume has suffered much more deformation at the higher Re, which can be interpreted as being largely due to a larger dimensional velocity (for fixed step height). As time proceeds, the $Re = 10$ case shows no "roll-up" of concentration contours in the recirculation zone. This is a direct consequence of the fact that at $Re = 10$, the much smaller recirculation zone contains little uncontaminated fluid until the contam-
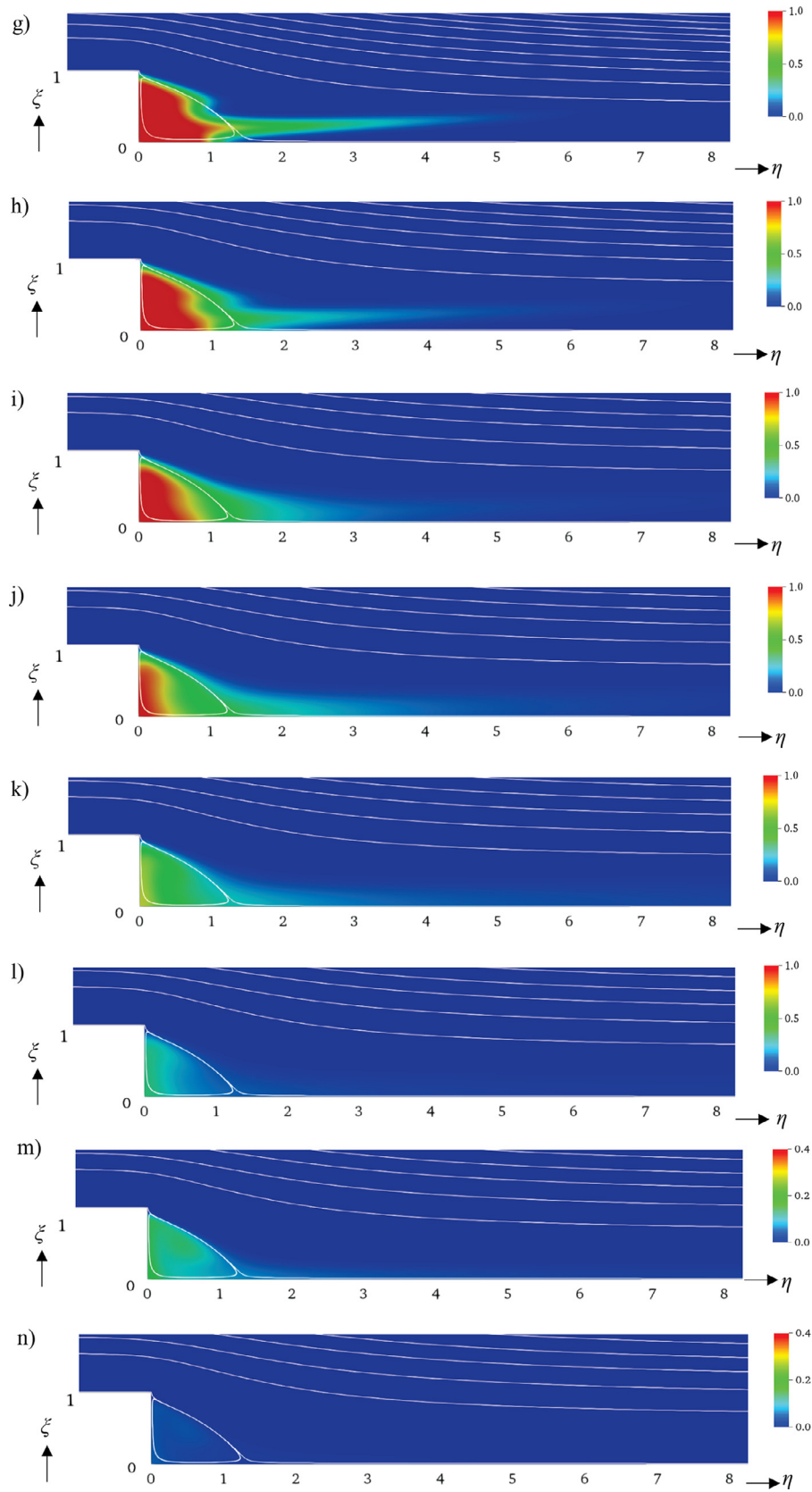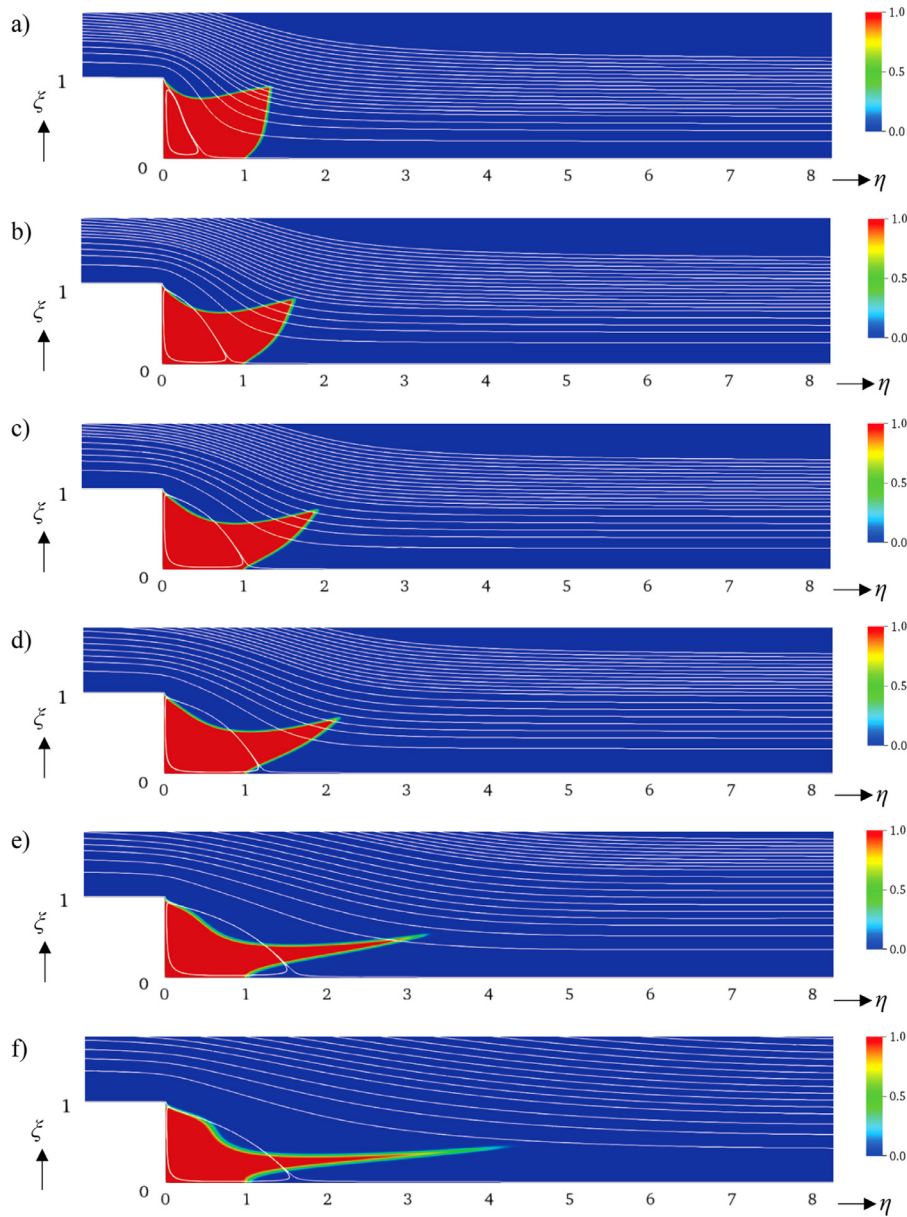
Fig. 8. Continued

Fig. 9. Evolution of streamlines (white lines) and contaminant distributions for $Re = 10$ and $Sc = 2650$ at a) $\tau_U = 0.5$, b) $\tau_U = 1$, c) $\tau_U = 1.5$, d) $\tau_U = 2$, e) $\tau_U = 5$, f) $\tau_U = 10$, g) $\tau_U = 25$, h) $\tau_U = 50$, i) $\tau_U = 100$, j) $\tau_U = 250$, k) $\tau_U = 500$, l) $\tau_U = 1000$. (For interpretation of the references to color in this figure legend, the reader is referred to the web version of this article.)

inant has been largely washed away. Thus, the recirculating flow does not lead to interleaved laminae of high and low concentration. In contrast, at $Re = 100$, the recirculation zone grows to include significant amounts of uncontaminated and highly contaminated fluid (cf. Fig. 3(c)), which are entrained in alternating laminae.

We can also compare Figs. 8(e) and 3(g) for $Sc = 500$ and Figs. 9(e) and 4(g) for $Sc = 2650$ (all at the same dimensional time, if Re is varied by changing U_∞). At $Re = 100$, mixing has been quite effective, with only a small zone of concentrated fluid remaining along the $\eta = 0$ wall, whereas at $Re = 10$, most of the contaminant remains undiluted in its original material volume. Supplemental Movie 3 shows that for $Re = 10$, evolution of the concentration distribution is dominated by recession of the highest-concentration region into a small part of the recirculation zone adjacent to the $\eta = 0$ wall, with much less structure to the distribution than for $Re = 100$.

For $Re = 10$, the concentration distributions for $Sc = 2650$ again show the effect of less diffusion compared to the $Sc = 500$ case

(see the thin "green" border between the highly contaminated fluid and the free-stream). Comparison of Figs. 8(g–i) to Figs. 9(g–i) shows that for $25 \leq \tau_U \leq 100$, the $Sc = 2650$ concentration distributions have more sharply defined features, with the smaller diffusivity leading to considerably more structure in the concentration distributions for the higher Sc at larger times (compare Figs. 8(m) and 9(m) at $\tau_U = 2000$).

Concentration distributions on the surface. For $Re = 10$, comparison of Figs. 10(a,b) for $Sc = 500$ and 2650, respectively, to the corresponding $Re = 100$ results of Figs. 5(a,b), shows that at high Sc the surface distribution for $Re = 10$ is significantly broadened downstream of $\eta = \sigma - 39 = 1$, compared to the $Re = 100$ case. This is a direct consequence of the fact that when τ_U is less than about 100, the contaminant concentration in the recirculation zone is fairly high for $Re = 100$, with contaminant transported outward across the separation streamline and then being carried downstream and wallward to a region near the reattachment point. In contrast, Figs. 8(a–i) and 9(a–i) (for $Sc = 500$ and 2650, respectively) show that the region of highest concentration has been
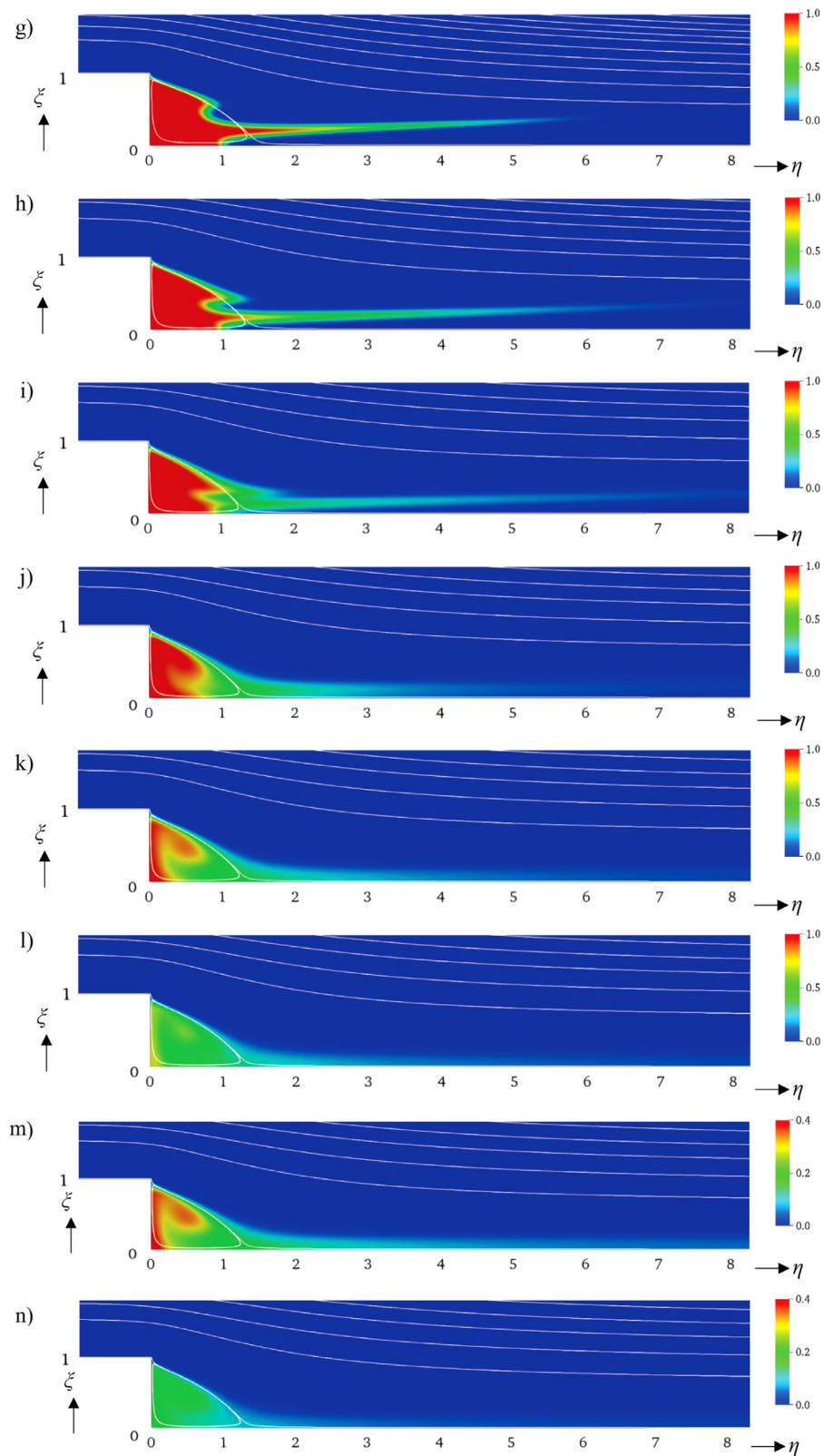
Fig. 9. Continued

greatly reduced (to a small region near the lower corner and the $\eta = 0$ wall) during a period ($0 \leq \tau_U \leq 100$) in which there is very little transport across the separation streamline.

A second notable difference between the surface concentration distributions for $Re = 100$ and $Re = 10$ is the significant nar-

rowing to the lower corner of the step that occurs beyond about $\tau_U = 250$ for the higher Re. This has no counterpart at any time for the $Re = 10$ case (Figs. 10(a,b)), and results from the fact that the higher-Re flow scours near-surface fluid on the $\eta = 0$ and $\xi = 0$ walls more efficiently. In contrast, for $Re = 10$, diffusion from the

a)

b)
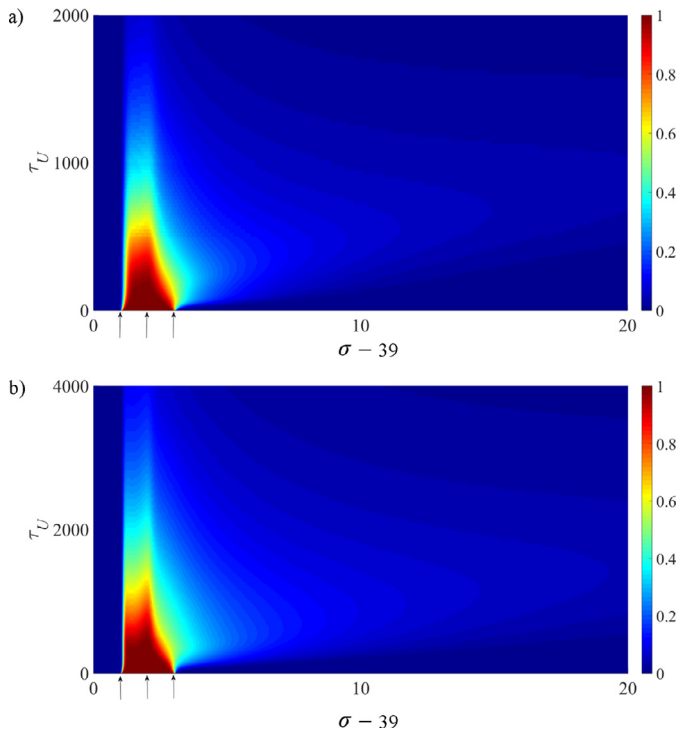
Fig. 10. For $Re = 10$ and a) $Sc = 500$ and b) $Sc = 2650$, time history of concentration along the wall. Left, center, and right arrows denote top corner of step (arclength $\sigma = 40$), bottom corner ($\sigma = 41$), and streamwise extent of initial contaminant distribution ($\sigma = 42$), respectively. Note the difference in time axes. (For interpretation of the references to color in this figure legend, the reader is referred to the web version of this article.)

bottom corner of the step into the central part of the recirculation zone is relatively more important, so that the concentration in the bottom corner is reduced more uniformly than in the $Re = 100$ case.

Maximum remaining concentration. For $Re = 10$ and $Sc = 500$, Fig. 11 (and Fig. S5 for the viscous time scale) shows that, in contrast to the situation at $Re = 100$ (Fig. 6, and Fig. S1 for the viscous time scale), the variation of S_{max} with time shows no discontinuity in slope, there being no time at which the maximum concentration shifts from the bottom corner of the step to the interior of the recirculation zone.

Integral measure of washout. For $Re = 10$ and $Sc = 500$ or 2650, Figs. 12(a,b) (and Figs. S6(a,b) for the viscous time scale) show that for all η_e considered, the amount of remaining contaminant decays nearly exponentially in time, with decay rates fitted to the data by linear least-squares given in Tables S6(a,b). The decay rate for $Sc = 500$ is larger than for $Sc = 2650$ by a factor of about 2.5. For $Sc = 500$, Fig. 12(a) shows that for each η_e, the fraction of contaminant remaining decreases monotonically in time, in contrast to the $Re = 100$ case (Fig. 7(a)) for which the dependence is not monotonic at small times. The key difference between results for the two Reynolds numbers is that for $Re = 10$, the separation streamline never reaches even the smallest η_e considered, and so upstream transport of contaminant into the region $\eta < \eta_e$ cannot occur.

3.3. Comparison to results at $Sc = 7$

Here, we compare the results presented above to results at $Sc = 7$, providing a connection to heat transfer, where the analog of Sc is the Prandtl number, which is almost exactly 7 for liquid water at 20 °C.

3.3.1. $Re = 100$, $Sc = 7$

Concentration distributions in the fluid. At $Re = 100$, comparison of Figs. 13(a–k) for $Sc = 7$ to results for $Sc = 500$ (Figs. 3(a–k)) and 2650 (Figs. 4(a–k)) clearly shows the effects of smaller Sc. The clearest difference is that the concentration distributions (see also Supplemental Movie 5) are much more diffuse at $Sc = 7$, and removal of contaminant from near the bottom of the step and from near the $\eta = 0$ wall (mediated by diffusion into the recirculation zone, and subsequent transport across the separation streamline into the outer flow) is greatly accelerated compared to the higher Sc cases.

Concentration distributions on the surface. Fig. 14 shows the spatiotemporal variation of the surface concentration for $Re = 100$ and $Sc = 7$. Comparison to the corresponding results at larger Sc (Figs. 5(a,b)) shows that the distribution is qualitatively different from those at higher Sc. Just downstream of $\eta = 1$ ($\sigma = 42$), the surface concentration increases for a while, but by $\tau_U = 12$ has started to decrease. Fig. 14 also shows that the upper portion of the $\eta = 0$ wall begins to "clear" of contaminant at very early times, indicated by appearance of a thin yellow zone for σ slightly greater than 40. We note that the surface concentration distribution is not even approximately "self-similar" to the distributions at higher Sc.

Maximum remaining concentration. For $Re = 100$ and $Sc = 7$, Fig. 6 (and Fig. S1 for the viscous time scale) shows that at each η_e, the plot of maximum concentration versus time does not undergo a step change in its slope, unlike the $Sc = 500$ and 2650 cases at this Re. This, and the comparatively much faster decrease of S_{max}, are directly attributable to the higher diffusivity. The asymptotic decay of S_{max} to nearly zero is much faster at $Sc = 7$ than at the higher Sc values considered.

Integral measure of washout. For $Re = 100$ and $Sc = 7$, Fig. S7 (and Fig. S8 for the viscous time scale) shows that after an initial transient for each η_e, M decays exponentially in time, with decay rate nearly independent of η_e (with numerical values provided in Table S7). At $Sc = 7$, the decay rate at each η_e is initially greater than its asymptotic value, and for $\eta_e \leq 20$ the asymptotic value of the decay rate is approached monotonically in time, whereas for $\eta_e = 40$, the decay rate passes through a minimum before approaching its asymptotic value.

3.3.2. $Re = 10$, $Sc = 7$

Concentration distributions in the fluid. For $Re = 10$ and $Sc = 7$ Supplemental Movie 6a shows that washout occurs very rapidly, and is essentially complete by the time the velocity field has reached a steady state. Supplemental Movie 6b, in which a much larger portion of the downstream domain is shown, and in which the false-color scheme changes with time, shows that as the maximum concentration decreases, its location moves continuously downstream, much as would a transient "burst" of heat or concentration in a flat-plate boundary layer. Note that beyond the streamwise location of the reattachment point, the cross-stream velocity component is directed away from that wall, and so the thickness of the high-concentration zone (in red) grows downstream due to both convection and diffusion.

For $Re = 10$ comparison of $Sc = 7$ results (Figs. 15(a–i)) to those for $Sc = 500$ (Figs. 8(a–i)) and 2650 (Figs. 9(a–i)) again shows the effects of smaller Sc. Concentration distributions much more diffuse at $Sc = 7$ and contaminant removal from the bottom of the step and from the $\eta = 0$ wall is greatly accelerated compared to the results at higher Sc.

Because the streamwise extent of the recirculation zone is considerably smaller for $Re = 10$ than for 100, contaminant diffusing away from the step for $Sc = 7$ finds a smaller recirculation zone for $Re = 10$ which it more readily fills, than in the $Re = 100$ case, as shown by comparison of Figs. 15(a–e) to Figs. 13(a–d). (Note
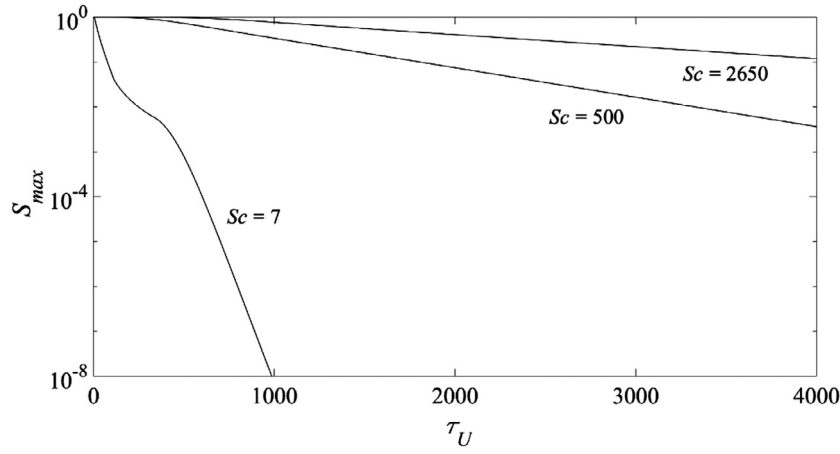
Fig. 11. Temporal variation of maximum concentration in the computational domain for $Re = 10$ and the three Schmidt numbers considered. Figure S5 presents these results using the viscous time scale τ_v.
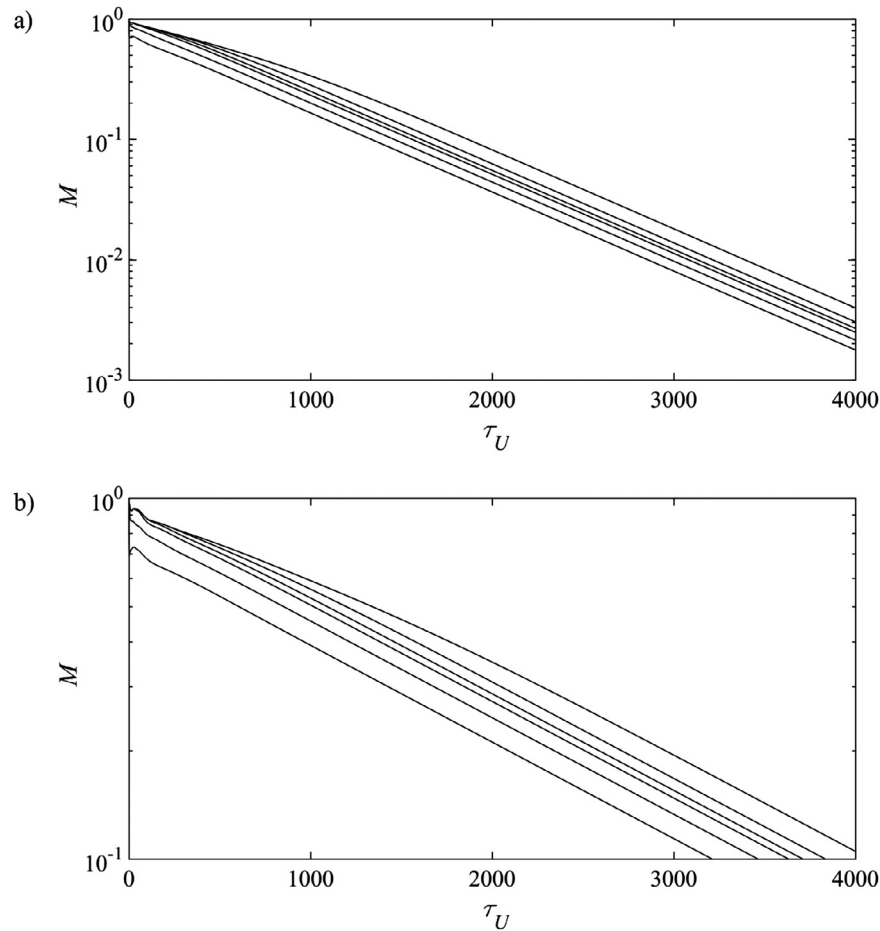

Fig. 12. For $Re = 10$ and a) $Sc = 500$ and b) $Sc = 2650$, time history of contaminant remaining upstream of a given η_e, for $\eta_e = 1$ (bottom curve), 2, 5, 10, 20, and 40 (top curve). Figures S6(a,b) present these results using the viscous time scale τ_v.

in Figs. 13(b–d) that a significant part of the recirculation zone is comprised of highly contaminated fluid.)

Concentration distributions on the surface. Fig. 16 shows spatiotemporal variation of surface concentration for $Re = 10$ and $Sc = 7$. For this case, with the smallest Péclet number ($Pe = 70$) of any considered, there is still no sensible diffusion of contaminant upstream of the step. Compared to the $Re = 100$, $Sc = 7$ case (Fig. 14), we see that once the upper portion of the $\eta = 0$ wall begins to

clear, the surface distribution for $Re = 10$, $Sc = 7$ is much smoother at each time than the corresponding distributions for higher Sc, and on the part of the $\eta = 0$ wall initially in contact with contaminant, the distribution is less peaked, due to much more rapid diffusion.

Maximum remaining concentration. For $Re = 10$ and $Sc = 7$, Fig. 11 (and Fig. S5 for the viscous time scale) shows that decay of S_{max} undergoes two changes in slope. We identified three disjoint
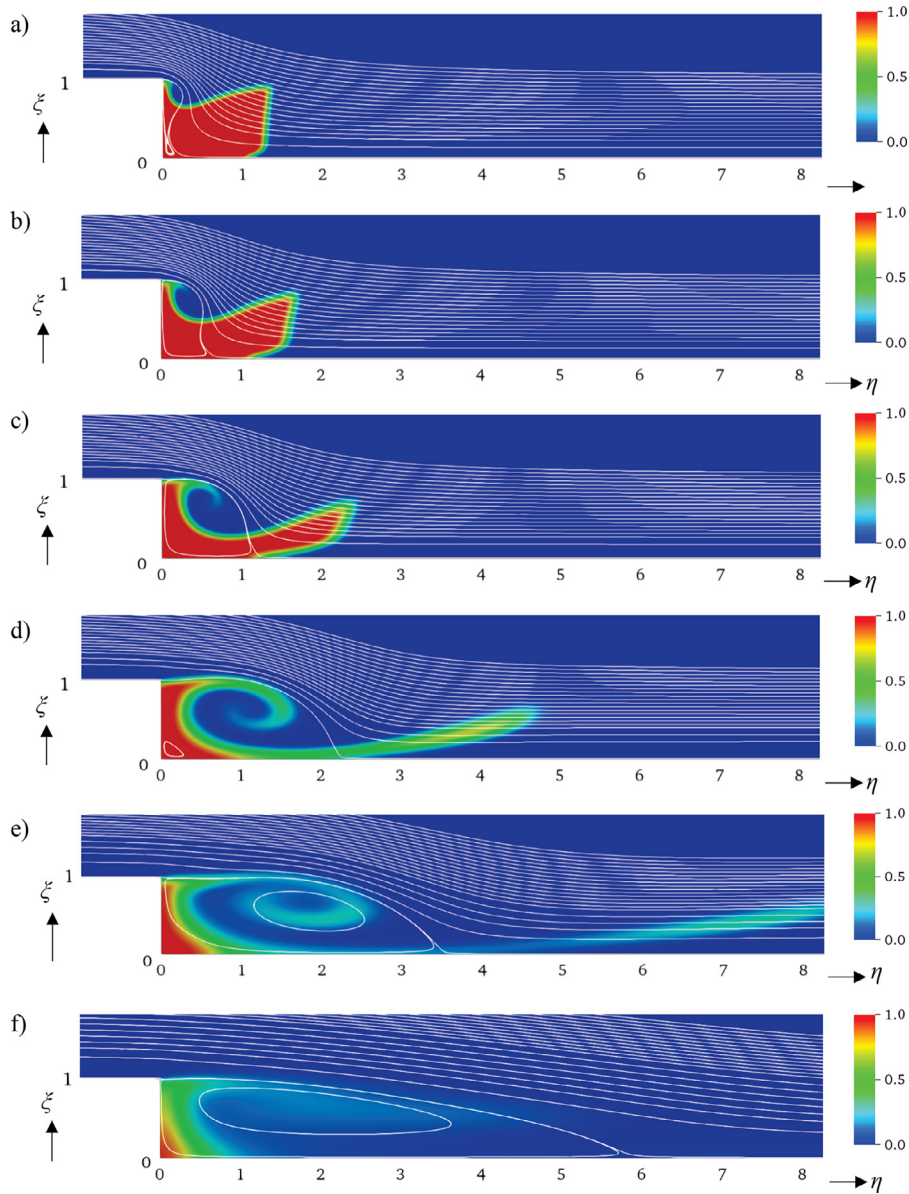
Fig. 13. Evolution of streamlines (white lines) and contaminant distributions for $Re = 100$ and $Sc = 7$ at a) $\tau_U = 0.5$, b) $\tau_U = 1$, c) $\tau_U = 2$, d) $\tau_U = 5$, e) $\tau_U = 10$, f) $\tau_U = 25$, g) $\tau_U = 50$, h) $\tau_U = 100$, i) $\tau_U = 250$, j) $\tau_U = 500$, k) $\tau_U = 1000$. (For interpretation of the references to color in this figure legend, the reader is referred to the web version of this article.)

time intervals in which the decay was nearly exponential, fitted a straight line to the semi-log plot in each interval, and then computed the intersections of the straight lines in the intervening time intervals (Fig. S11). This gives "transition times" of approximately $\tau_U = 115$ and 488 for the slope changes. These correspond closely to the times at which the maximum concentration point switches from the bottom corner of the step to the $\xi = 0$ wall ($\tau_U \approx 113$) and the time at which the maximum concentration point passes out of the computational volume ($\tau_U \approx 480$). Beyond the latter time, the maximum concentration in the computational domain again occurs at the bottom corner of the step. We note that the decay rates are quite similar for $\tau_U < 113$ and for $\tau_U > 480$, in both cases associated with diminution of the concentration at the bottom corner of the step.

For $Sc = 7$, comparison of Figs. 6 and 11 shows that S_{max} decreases to zero more rapidly with time at $Re = 10$ than at $Re = 100$, owing to the smaller recirculation zone, discussed above in connection with the concentration distributions in the fluid.

Integral measure of washout. For $Re = 10$ and $Sc = 7$, the plot of M versus τ_U in Fig. S10 (and Fig. S11 for the viscous time scale) shows that the rate of decay of the integral measure M is orders of magnitude faster than for the previously considered cases. After initial transients (which progressively shorten as η_e increases), M decays nearly exponentially in time for each η_e with a decay rate independent of η_e (numerical values are provided in Table S8). Unlike the $Re = 100$, $Sc = 7$ case, the decay rate at each η_e is initially lower than its asymptotic value. As for $Re = 100$, $Sc = 7$, the asymptotic decay rate is approached monotonically in time for $\eta_e = 1$, whereas for $\eta_e = 40$, the decay rate exhibits a minimum before approaching its asymptotic value.
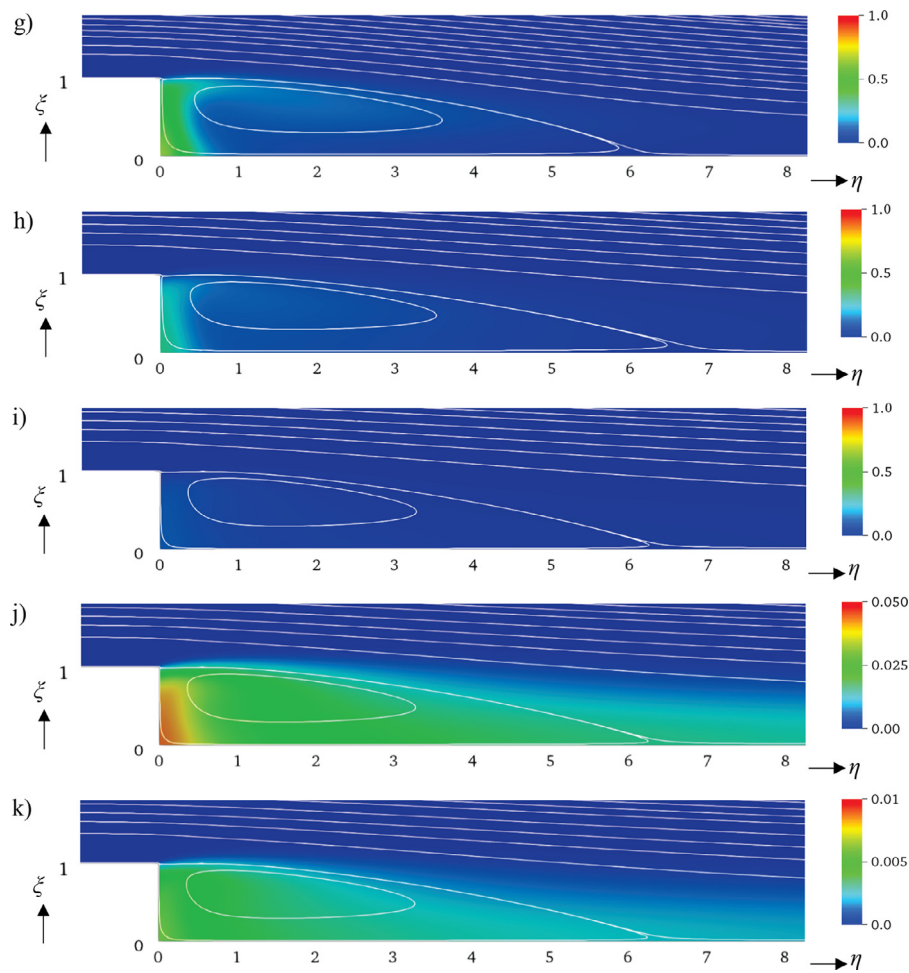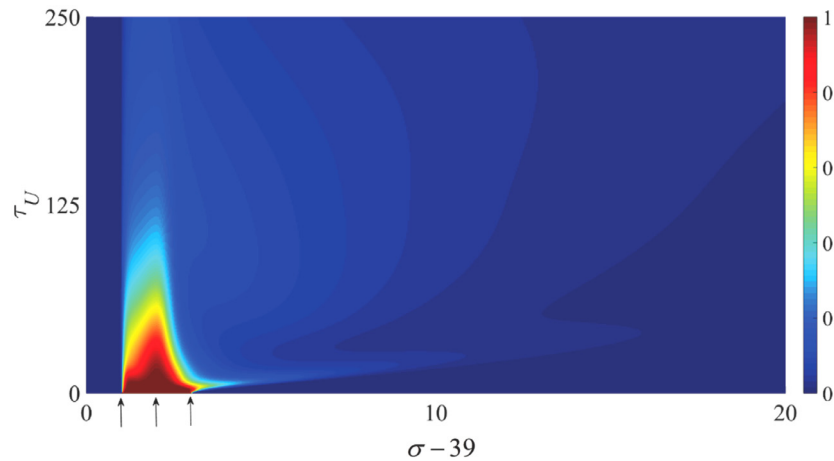
Fig. 13. Continued

Fig. 14. For $Re = 100$ and $Sc = 7$, time history of concentration along the wall. Left, center, and right arrows denote top corner of step (arclength $\sigma = 40$), bottom corner ($\sigma = 41$), and streamwise extent of initial contaminant distribution ($\sigma = 42$), respectively. (For interpretation of the references to color in this figure legend, the reader is referred to the web version of this article.)

4. Discussion

For all cases considered, the time dependence of the maximum concentration (S_{max}) and the contaminant remaining upstream of a specified streamwise location M can be closely approximated by single exponentials after some initial transient. For $Re = 100$ and $Sc = 500$ or 2650, the initial transient for S_{max} includes times dur-

ing which the maximum concentration is at the bottom corner of the step, when S_{max} can be approximated by a different single exponential.

For $Re = 100$ and either $Sc = 500$ or 2650, the maximum concentration shifts from its initial location at the bottom corner of the step to the interior of the recirculation zone, accompanied by an abrupt change in the slope of S_{max} versus time. This shift does
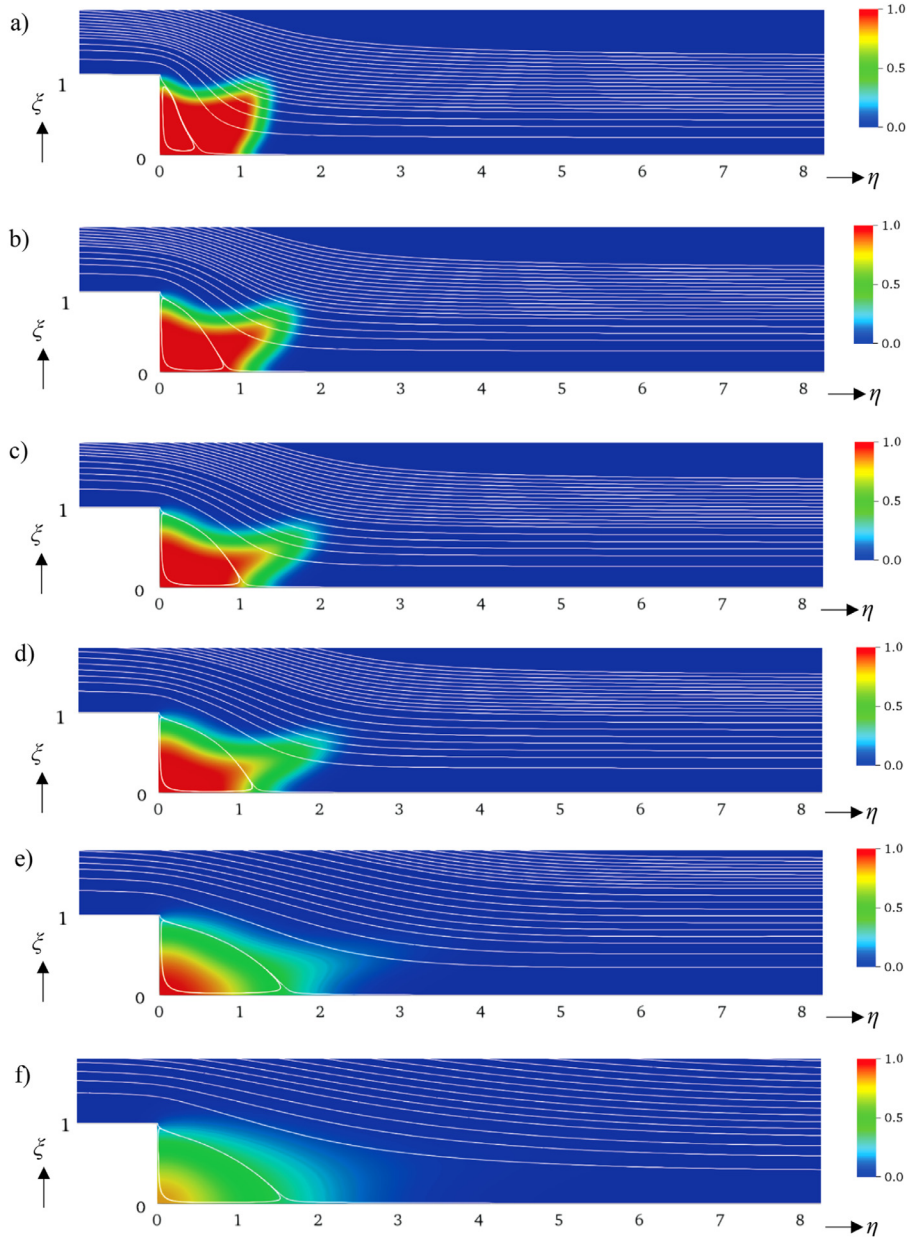
Fig. 15. Evolution of streamlines (white lines) and contaminant distributions for $Re = 10$ and $Sc = 7$ at a) $\tau_U = 0.5$, b) $\tau_U = 1$, c) $\tau_U = 1.5$, d) $\tau_U = 2$, e) $\tau_U = 5$, f) $\tau_U = 10$, g) $\tau_U = 25$, h) $\tau_U = 50$, i) $\tau_U = 100$. (For interpretation of the references to color in this figure legend, the reader is referred to the web version of this article.)

not occur for $Re = 10$ at either of these Sc values. For $Re = 10$ and $Sc = 7$, the results are fitted using three piecewise exponentials.

At $Re = 10$, comparison of results for the integral measure M shows that washout is orders of magnitude faster at $Sc = 7$ than at 500. That results for these Sc values differ much less at $Re = 100$ illustrates the important influence of flow, and shows that inferences about applicability of low-Sc results to high-Sc cases can depend strongly on Re, even when the Péclet numbers in both cases are relatively large. In the comparison above, the important issue is not the Péclet number, but rather the size of the recirculation zone in this nonparallel flow. More generally, the results suggest that for other topographies (e.g., the three-dimensional obstacle of Boum et al. [21] with $500 \leq Sc \leq 2000$), the disparity between low- and high-Sc results will likely depend on Re. There are no results in the literature for $Pr = 7$ (or $Sc = 7$) that can be compared to those of [21], which is not surprising given the reactive boundary condition considered in that work.

The washout results for M vs. τ can be correlated with Re and Sc as follows. We begin by considering the exponential decay rates shown in Tables S5-S8 for the six combinations of Re and Sc investigated. Choosing the decay rates at $\eta_e = 10$ (denoted by β_{10}), we then consider a simple power-law correlation of the form $\beta_{10} = cRe^a Sc^b$. We then perform a logarithmic transformation and divide by β_{10} to get the least-squares problem of minimizing

$$E = \sum_{i=1}^{6} \left[\frac{a \ln Re_i}{(\beta_{10})_i} + \frac{b \ln Sc_i}{(\beta_{10})_i} + \frac{F}{(\beta_{10})_i} - 1 \right]^2 \tag{9}$$

where $F = \ln c$. (We have divided by β_{10} so as to equally weight the square of the relative error for each combination of Re and Sc. If we had not done so, the fit would've reduced the error for the largest β_{10} at the expense of the other cases.). The resulting fit is $\beta_{10} = 0.4783 Re^{-0.7791} Sc^{-0.6227}$. The average and maximum values of the error (the magnitude of the term within the square brackets
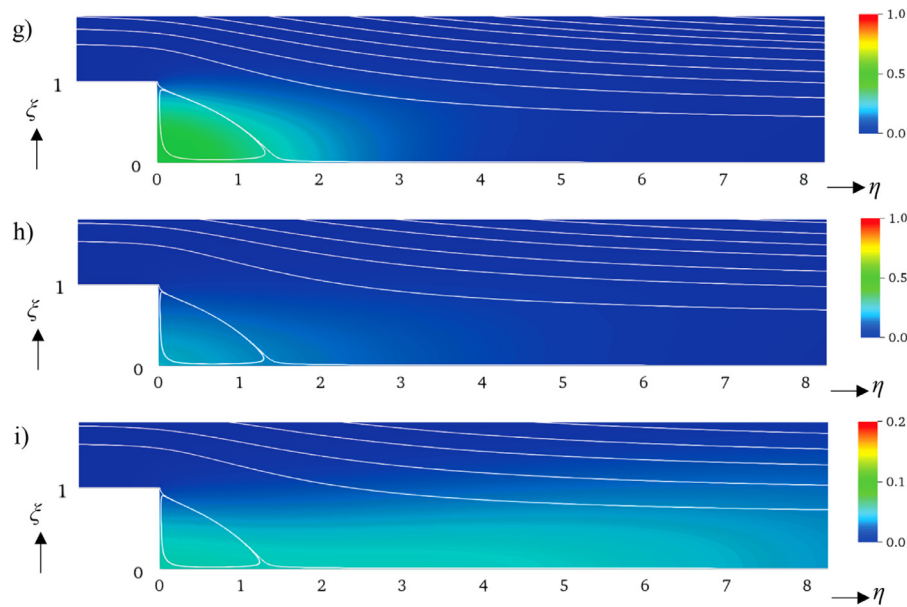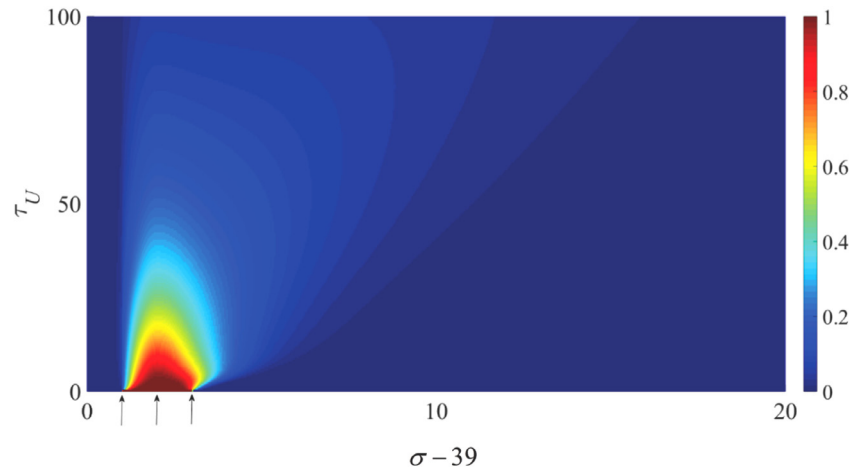
Fig. 15. Continued

Fig. 16. For $Re = 10$ and $Sc = 7$, time history of concentration along the wall. Left, center, and right arrows denote top corner of step (arclength $\sigma = 40$), bottom corner ($\sigma = 41$), and streamwise extent of initial contaminant distribution ($\sigma = 42$), respectively. (For interpretation of the references to color in this figure legend, the reader is referred to the web version of this article.)

in Eq. (9)) over the six combinations of Re and Sc are 0.7% and 1.4%, respectively. Of course, using a three-parameter fit to correlate six data points provides no assurance that the fit works well either between the available points or beyond them.

Our results, for the case in which contaminant is initially confined to a square region immediately downstream of the step, provide at least qualitative insight into situations in which a contaminant is shielded or "harbored" by more complex topographical features (e.g., roughness elements of finite streamwise or spanwise extent). (Our initial conditions and the no-flux condition on the wall precludes direct comparison of our $Sc = 7$ results to any $Pr = 7$ results in the literature.) Among other things, the results demonstrate the slowness with which contaminant shielded by protective topography is removed by a flow that passes over the topography. These results point to the importance of washing approaches that direct flow directly onto protective topography. Although our results pertain to an idealized geometry, they are expected to provide guidance in assessing the time required to wash out shielded contaminant in a number of applications.

We fully expect that a power-law correlation of the form considered above will apply for a variety of initial solute distributions, with different values of the fitted coefficients.

5. Conclusion

The results presented in §3 at $Sc = 500$ and 2650 appear to be the first detailed computations for mass transfer past a backward-facing step in a laminar flow at Schmidt numbers this high (or for convective heat transfer at correspondingly high Prandtl numbers), and show that washout is considerably retarded compared to smaller Sc. The joint effects of flow and diffusion on solute transport are in some cases quite striking, and clearly demonstrate the subtle interplay between these transport mechanisms, and illustrate the importance of Reynolds number and Schmidt number effects in the laminar regime. The results also emphasize the importance of using a computational approach capable of resolving strong gradients in the concentration field with reasonable computational effort. The rate at which the amount of solute upstream

of a fixed streamwise location decays in time is very nicely fitted by a simple power-law correlation.

Finally, this work conclusively shows that results for $Pr = 7$ provide a poor guide for high-Sc convective mass transfer in liquids.

Declaration of Competing Interest

The authors declare that they have no financial, organizational, familial, or other conflicts of interest.

CRediT authorship contribution statement

Dahhea Min: Formal analysis, Methodology, Software, Validation, Visualization, Writing - original draft, Writing - review & editing. **Paul F. Fischer:** Methodology, Software, Validation, Writing - review & editing. **Arne J. Pearlstein:** Funding acquisition, Methodology, Validation, Writing - original draft, Writing - review & editing.

Acknowledgments

Supplementary materials

Supplementary material associated with this article can be found, in the online version, at doi:10.1016/j.ijheatmasstransfer.2020.119740.

References

[1] M.I. Gil, M.V. Selma, F. López-Galvez, A. Allende, Fresh-cut product sanitation and wash water disinfection: problems and solutions, Int. J. Food Microbiol. 134 (2009) 37–45.

[2] A.A. Bhagwat, Microbial safety of fresh-cut produce: where are we now?, in: Microbiology of Fresh Produce, Chapter 5, Amer, Soc. Microbiol. (2006).

[3] S. Weng, Y. Luo, J. Lie, B. Zhou, J.G. Jacangelo, K.J. Schwab, Assessment and speciation of chlorine demand in fresh-cut produce wash water, Food Control 60 (2016) 543–551.

[4] European Commission (EC). Regulation (EU) No 528/2012 of the European parliament and of the council of 22May 2012concerning the making available on the market and use of biocidal products. Available online: https://eur-lex.europa.eu/legal-content/EN/TXT/?uri=CELEX%3A32012R0528 (accessed on 18 June 2020).

[5] Food and Drug Administration (FDA). Code of Federal Regulations. Sec. 173.300 Chlorine dioxide. Available online: http://www.accessdata.fda.gov/scripts/cdrh/cfdocs/cfcfr/CFRSearch.cfm?fr=173.300 (accessed on 14 April 2015).

[6] Y. Luo, B. Zhou, P.D. Millner, A.J. Pearlstein, System for cleaning fresh and fresh-cut produce, U.S. Patent 10,285,411 (issued May 14, 2019).

[7] W. Aung, An experimental study of laminar heat transfer downstream of back-steps, J. Heat Trans. (Trans. ASME) 105 (1983) 823–829.

[8] J.C. Vogel, J.K. Eaton, Combined heat transfer and fluid dynamic measurements downstream of a backward-facing step, J. Heat Trans. (Trans. ASME) 107 (1985) 922–929.

[9] E.V. Shishov, P.S. Roganov, S.I. Grabarnik, V.P. Zablotsky, Heat transfer in the re circulating region formed by a backward-facing step, Int. J. Heat Mass Trans. 31 (1988) 1557–1562.

[10] T. Kondoh, Y. Nagano, T. Tsuji, Computational study of laminar heat transfer downstream of a backward-facing step, Int. J. Heat Mass Trans. 36 (1993) 577–591.

[11] E. Achenbach, Mass transfer downstream a backward or a forward-facing step, in Proc, in: G. Hetsroni (Ed.), 9th Intl. Heat Transfer Conf., Jerusalem, 5, Hemisphere, New York, 1990, pp. 305–310.

[12] B.F. Boyarshinov, On the boundaries of the transitional regime of mass transfer during ethanol combustion on horizontal rear walls of a rib and a step, Combust. Expl. Shock Waves 51 (2015) 401–408.

[13] G. Rappitsch, K. Perktold, Computer simulation of convective diffusion, J. Biomech. 29 (1996) 207–215.

[14] K.B. Hansen, S.C. Shadden, A reduced-dimensional model for near-wall transport in cardiovascular flow, Biomech. Model. Mechanobiol. 15 (2016) 713–722.

[15] E.M. Lutostansky, G. Karner, G. Rappitsch, D.N. Ku, K. Perktold, Analysis of hemodynamic fluid phase mass transfer in a separated flow region, J. Biomech. Eng. 125 (2003) 189–196.

[16] L. Wang, X.-Y. Lu, An investigation of turbulent oscillatory heat transfer in channel flows using large eddy simulation, Int. J. Heat Mass Trans. 47 (2004) 2161–2172.

[17] C. Scalo, U. Piomelli, L. Boegman, Self-similar decay and mixing of a high-Schmidt-number passive scalar in an oscillating boundary layer in the intermittently turbulent regime, J. Fluid Mech. 726 (2013) 338–370.

[18] P.M. Le, D.V. Papavassiliou, Turbulent dispersion from elevated line sources in turbulent channel and Couette flow, AIChE J. 51 (2005) 2402–2414.

[19] E. Kaminski, C. Jaupart, Laminar starting plumes in high-Prandtl-number fluids, J. Fluid Mech. 478 (2003) 287–298.

[20] H.-.L. Tran, A. Sergent, G. Bernard-Michel, P. Le Quéré, Numerical Study of Starting Plumes At High Schmidt number, 21eme Congr. Français Méc., Bordeaux, 2013.

[21] G.B.N. Boum, S. Martemianov, A. Alemany, Computational study of laminar flow and mass transfer around a surface-mounted obstacle, Int. J. Heat Mass Trans. 42 (1999) 2849–2861.

[22] P. Olivas, S. Zahrai, F.H. Bark, On unsteady electrochemical coating of a cylinder at moderately large Reynolds number, J. Appl. Electrochem. 27 (1997) 1369–1379.

[23] C.-J. Hsu, An exact analysis of low Peclet number thermal entry region heat transfer in transversely nonuniform velocity fields, AIChE J. 17 (1971) 732–740.

[24] H. Schlichting, in: Boundary-Layer Theory, 6th Edition, McGraw-Hill, New York, 1968, p. 129.

[25] H. Fasel, U. Konzelmann, Non-parallel stability of a flat-plate boundary layer using the complete Navier-Stokes equations, J. Fluid Mech. 221 (1990) 311–347.

[26] D. Lanzerstorfer, H.C. Kuhlmann, Global stability of the two-dimensional flow over a backward-facing step, J. Fluid Mech. 693 (2012) 1–27.

[27] A.T Patera, A spectral element method for fluid dynamics - laminar flow in a channel expansion, J. Comp. Phys. 54 (1984) 468–488.

[28] P.F. Fischer, J.W. Lottes, S.G. Kerkemeier, Nek5000, https://nek5000.mcs.anl.gov (accessed on 5 May 2020).

[29] Y. Maday, A.T. Patera, ASME, New York, 1989, pp. 71–143.

[30] P.M. Gresho, D.K. Gartling, J.R. Torczynski, K.A. Cliffe, K.H. Winters, T.J. Garratt, A. Spence, J.W. Goodrich, Is the steady viscous incompressible two-dimensional flow over a backward-facing step at $Re = 800$ stable? Int. J. Numer. Methods Fluids 17 (1993) 510–541.

[31] M.S. Chao, The diffusion coefficients of hypochlorite, hypochlorous acid, and chlorine in aqueous media by chronopotentiometry, J. Electrochem. Soc. 115 (1968) 1172–1174.

[32] J. Kestin, M. Sokolov, W.A. Wakeham, Viscosity of liquid water in the range -8°C to 150°C, J. Phys. Chem. Ref. Data 7 (1978) 941–948.